Elemental and oxygen isotopic fractionation recorded in highly vaporized cosmic spherules from Widerøefjellet, Sør Rondane Mountains (East Antarctica)

Tom Boonants[1*], Steven Goderis[1], Bastien Soens[1], Flore Van Maldeghem[1], Stepan M. Chernonozhkin[2,3], Frank Vanhaecke[2], Matthias van Ginneken[4], Christophe Snoeck[1], Philippe Claeys[1]

[1] Archaeology, Environmental Changes & Geo-Chemistry, Vrije Universiteit Brussel, Pleinlaan 2, B-1050 Brussels, Belgium

[2] Department of Chemistry, Atomic & Mass Spectrometry A&MS research unit, Ghent University, Campus Sterre, Krijgslaan 281 – S12, B-9000 Ghent, Belgium

[3] Chair of General and Analytical Chemistry, Montanuniversität Leoben, Franz Josef Straße 18, 8700 Leoben, Austria

[4] Centre for Astrophysics and Planetary Science, School of Physical Sciences, University of Kent, Canterbury CT2 7NH, UK

* Corresponding author. Email address: Tom.Boonants@vub.be

Abstract

Upon passage through Earth's atmosphere, micrometeorites undergo variable degrees of melting and evaporation. Among the various textural and chemical groups recognized among cosmic spherules, i.e. melted micrometeorites, a subset of particles may indicate anomalously high degrees of vaporization based on their chemical and isotopic properties. Here, a selection of such refractory element-enriched cosmic spherules from Widerøefjellet (Sør Rondane Mountains, East Antarctica) is characterized for their petrographic features, major and trace element concentrations (N = 35), and oxygen isotopic compositions (N = 23). Following chemical classification, the highly vaporized particles can be assigned to either the 'CAT-like' or the 'High Ca-Al' cosmic spherule groups. However, through combination of major and trace element concentrations and oxygen isotopic data, a larger diversity of processes and precursor materials are identified that lead to the final compositions of refractory element-enriched particles. These include fragmentation, disproportional sampling of specific mineral constituents, differential melting, metal bead extraction, redox shifts, and evaporation. Based on specific element concentrations (e.g., Sc, Zr, Eu, Tm) and ratios (e.g., Fe/Mg, $CaO+Al_2O_3/Sc+Y+Zr+Hf$), and variations of O isotope compositions, 'CAT-like' and 'High Ca-Al' cosmic spherules likely represent a continuum between mineral end-members from both primitive and differentiated parent bodies that experienced variable degrees of evaporation.

1. Introduction

Of the 40 ± 20 thousand metric tons of cosmic matter that accumulate on Earth annually (Love & Brownlee, 1993), the majority arrives in the form of micrometeorites (Suttle & Folco, 2020; Taylor et al., 1998), which are extraterrestrial particles in the size range of 10 to 2,000 µm (Rubin & Grossman, 2010). These micrometeorites are thought to mainly represent microscopic samples of asteroids and comets that have been captured by Earth's gravity (Genge, 2006) and exist in a wide variety of shapes, sizes, and petrographic types (Cordier & Folco, 2014; Genge et al., 2008; Suavet et al., 2010; Yada et al., 2005). The smaller size fractions (< 500 µm) of micrometeorites are thought to mainly relate to carbonaceous chondrites (CC) (Genge et al., 1997; Kurat et al., 1994). In the case of larger micrometeorites, a significant fraction appears to be linked to ordinary chondritic (OC) material, with a CC/OC-ratio of 10:1 at 10 µm diameter and a CC/OC below 1 in the case of particle diameters ≥1000 µm (Cordier & Folco, 2014). One major issue micrometeorite studies commonly face is that their mineralogical, geochemical, and isotopic properties do not entirely match those of their respective parent bodies (Brearley & Jones, 1998). This observation has been attributed to several reasons including: (i) parent body heterogeneity, as mineralogical and geochemical properties within the micrometeorite parent body may vary significantly on a microscopic scale (Genge et al., 1997; 2005), and (ii) alteration of the initial micrometeoroid properties due to atmospheric entry heating and terrestrial alteration (Cordier et al., 2011; Engrand et al., 2005; Love & Brownlee, 1991; van Ginneken et al., 2016; Taylor et al., 2005). Therefore, a thorough investigation using a combination of petrographic, geochemical and isotopic data is required to trace their original mineralogy and chemical composition.

Micrometeorites are generally categorized in three different classes, based on the degree of melting experienced during atmospheric entry (Genge et al., 2008), following the direct collision with gas molecules. The three main classes are: (i) melted micrometeorites (commonly referred to as 'cosmic spherules'), which are formed as molten droplets during atmospheric entry; (ii) partially melted micrometeorites (scoriaceous), which retain a distinct irregular shape, but clearly show indication of melting; and (iii) unmelted micrometeorites ('angular micrometeorites'), displaying no to very limited melted areas (Genge et al., 2008; Folco & Cordier, 2015; Maurette et al., 1994). Cosmic spherules can be further subdivided into iron-rich spherules (I-type; Genge et al., 2017), magnetite-rich spherules embedded in a glassy mesostasis (G-type; Blanchard et al., 1980; Genge, 2006), and silicate-type cosmic spherules (S-type; Genge, 2006). The S-type cosmic spherules are by far the most commonly recovered subcategory (97% of all cosmic spherules) (Genge, 2006; Taylor et al., 2000), and can be further subdivided into porphyritic (Po-type), barred olivine (BO-type), cryptocrystalline (CC-type) and vitreous (V-type) cosmic spherules based on their textures, which typically form a series that

represents a gradient of increased peak temperature experienced during atmospheric entry (Genge et al., 1997; Szydlik & Flynn, 1992). The differences in this peak temperature are reflected in the petrography and crystal sizes.

Besides the aforementioned types, CAT spherules have also been described in literature (Taylor et al., 2000), and are defined based on distinct textural characteristics, albeit with a characteristic accompanying chemical composition. They are oblate and white, and resemble barred olivine spherules, with the absence of magnetite (Taylor et al., 2000). Typically, they have a Mg/Al ratio of >1.7, isotopic compositions testify of isotopic fractionation, and they are enriched in Ca, Al and Ti relative to other S-type spherules (Taylor et al., 2000; Alexander et al., 2002). Cordier et al. (2011) proposed to subdivide V-type cosmic spherules into 'normal chondritic' spherules, 'CAT-like' spherules and 'High Ca-Al' spherules based on the chemical composition and presumed extent of evaporative loss experienced. These three defined subgroups display a progressive increase in refractory major and trace element contents (including Zr, Hf, Sc, Al, Y, and Ti). The observed deviations in refractory element content are caused by passive enrichment processes, after a fraction of more volatile (and moderately refractory) elements, such as Pb, Zn, Ba, Sr, and Fe, are lost through evaporation during atmospheric heating. The 'normal chondritic' spherules display the lowest degree of chemical fractionation, calculated to have lost 40–50% of their mass during atmospheric entry evaporation (Alexander et al., 2002). The lost mass fraction increases to 50-70% for 'CAT-like' spherules, while 'High Ca-Al' spherules are thought to have experienced 80-90% mass loss (Cordier et al., 2011). In a Fe/Si (atomic) vs CaO + Al_2O_3 (wt.%) diagram, the three defined subtypes cover well-defined areas (Fig. 1): (i) 'Normal chondritic' spherules plot in the lowest CaO + Al_2O_3 regions (CaO + Al_2O_3 values below 5 wt.% for atomic Fe/Si ratios < 0.04, and below 9 wt.% for atomic Fe/Si ratios > 0.04), (ii) 'CAT-like' spherules plot at CaO + Al_2O_3 values above 5 wt.%, with atomic Fe/Si ratios < 0.04, and (iii) 'High Ca-Al' spherules exhibit CaO + Al_2O_3 values above 9 wt.%, with atomic Fe/Si ratios > 0.04 (Cordier et al., 2011).

Although 'CAT-like' spherules are described in literature (Cordier et al., 2011) to be highly evaporated particles, it is important to highlight that they are discriminated from other cosmic spherules based on chemical criteria, rather than textural criteria. This classification system was originally proposed in a study that focused on V-type cosmic spherules (Cordier et al., 2011), but was later extended to a wider variety of petrographic types of cosmic spherules (CC, BO, Po; Goderis et al., 2020). The terms CAT and 'CAT-like' spherules thus reflect different classification systems, even though they both have been suggested to have experienced extensive degrees of evaporation. The evaporative mass losses for 'High Ca-Al' spherules (80-90%) supersede those of the CAT spherules (Cordier et al., 2011). These overall differences between various classification systems, along with potential overlap between various particle types, may lead to some degree of ambiguity, which represents an important argument

for revisiting this type of particles. Furthermore, this study aims to refine how highly evaporated ('highly vaporized') cosmic spherules are formed. The presented data provide a comprehensive study of highly vaporized cosmic spherules, improving our overall understanding of their parent body materials and the respective processes that affected them, and constrain the chemical modifications that these particles experienced following atmospheric entry.

2. Materials and methods

a. Sample selection & petrographic characterization

The samples used in this project were collected from Mount Widerøe (Widerøefjellet) (72°09'S, 23°17'E), Sør Rondane Mountains (Dronning Maud Land, East Antarctica) during the 2017-2018 BELAM field campaign. The Sør Rondane Mountains (SRM) cover a surface area of approximately 2000 km^2 and are presumed to have been geologically stable for the last 650-500 Myr (Shiraishi et al., 2008). The region surrounding the Belgian Princess Elisabeth Antarctica Station (71°57'S, 23°21'E) was studied using satellite images and geological maps before the start of the field campaign, as done during previous campaigns (e.g., Imae et al., 2015). The sedimentary traps in the SRM have previously been found to be enriched in extraterrestrial materials, reflecting a well-preserved and representative micrometeorite collection in East Antarctica characterized by distinct geological and exposure histories (Goderis et al., 2020, Van Maldeghem et al., 2023). Erosional and eolian sediment was sampled from exposed fissured and cracked surfaces at Widerøefjellet, where a total of 11.97 kg of detritus was collected (WF18 #01: 2.65 kg; WF18 #02: 3.17 kg; WF18 #03: 6.15 kg).

Following manual removal of the largest rock fragments, the sediment was gradually defrosted at the Princess Elisabeth Antarctica Station. Based on three different sieved non-magnetic fractions (size fractions 800-400 µm, 400-200 µm and 200-125 µm) from the same deposit (WF18 #01), a total of 78 cosmic spherules were randomly selected from ~200 spherules that appeared to be white to transparent in color, which is considered a typical characteristic for highly vaporized cosmic spherules (Alexander et al., 2002). All cosmic spherule extraction was done by manual picking using a Zeiss Stereo Discovery V20 optical microscope at the Archaeology, Environmental Changes & Geo-Chemistry (AMGC) research unit of the Vrije Universiteit Brussel (VUB). From this initial selection, the assortment was further refined using a JEOL JSM IT-300 Scanning Electron Microscope – Energy-Dispersive X-ray Spectrometer (SEM-EDS) system at the Electrochemical and Surface Engineering (SURF) research group of the VUB. A total of 35 spherules that exhibited the highest concentrations of refractory elements Ca, Al and Ti, displaying a variety of textures (Fig. 2), were extracted for further analysis. The combined color and chemical compositions support the likelihood of these particles being CAT spherules, as

defined by Taylor et al. (2000), or fit within the 'CAT-like' or 'High Ca-Al' chemical groups defined by Cordier et al. (2011) for glass particles. In total, the sample set consists of 12 V-type, 1 CC-type, 14 BO-type, 6 mixed CC/BO-type hybrid and 1 Po-type cosmic spherules. Furthermore, 1 sample was found to potentially be of scoriaceous nature, although it has no profound lobate shape (Fig. 2E).

b. Major and trace element compositions

After embedding in epoxy resin and polishing with sandpaper on a rotating disc, the selected cosmic spherules were analysed for major and trace element compositions using a LA-ICP-MS setup consisting of a Teledyne Photon Machines Analyte G2 ArF* excimer-based laser ablation system coupled to a Thermo Scientific Element XR double-focusing sector-field ICP-MS unit at the Atomic and Mass Spectrometry (A&MS) group at Ghent University (Belgium). The analytical procedure followed was adapted from Das Gupta et al. (2017) and Chernonozhkin et al. (2021). Analyses were performed in a spot analysis mode using a laser spot size 40 µm in diameter, a laser dwell time of 20 s (preceded by 15 s of pre-ablation at softer laser parameters and followed by 40 s wash-out), a repetition rate of 35 Hz, corresponding to 700 shots, and a beam energy density of 2.98 J/cm^2 on the sample surface. The particles and reference materials were mounted in a double-volume ablation cell (a standard HELEX 2). The He carrier gas (0.5 L/min) was mixed with Ar make-up gas downstream of the ablation cell, and subsequently introduced into the ICP-MS unit, which was operated in low mass resolution mode. Semi-cold plasma conditions (800 W RF power) were used for reducing Ar-based interferences. Quantification was achieved through external calibration using a set of glass reference materials with natural rock composition, GOR 128-G, ML3B-G, KL2-G, StHs6/80-G1-G, ATHO-G, T1-G and GOR 132-G (MPI-DING), and GSE-1G, BHVO-2G, GSD-1G, NKT-1G and BIR-1G (USGS). Daily tuning of the LA-ICP-MS parameters using NIST612 glass reference material was performed to maximize the sensitivity, minimize the formation of oxide and double-charged species, and to limit the elemental fractionation (*i.e.* $^{238}U^+/^{232}Th^+$ ratio close to 1). The intermediate precision for the element concentrations – expressed as the relative standard deviation (RSD) of five replicate measurements of basaltic glass BHVO-2G – was below 5%.

c. Oxygen isotope measurements

A total of 23 particles was analysed by Secondary Ion Mass Spectrometry (SIMS) at the Centre de Récherches Pétrographiques et Géochimiques (CRPG) in Nancy (France) for their oxygen isotopic composition. For this purpose, a CAMECA IMS 1270 was used, which applied a Cs^+ ion beam with a

spot size of approximately 15 µm. The beam was directed at the samples under an angle of 20 – 25°. Each main measurement consisted of 90 seconds pre-sputtering and 30 measurements of 5 seconds. The intensities for the oxygen isotopes (^{16}O, ^{17}O and ^{18}O) were determined using three Faraday cups. To avoid interference from ^{16}OH, ^{17}O was measured with an axial Faraday cup, with the exit slit width corresponding to a mass resolution of 7000. The ^{16}O and ^{18}O isotopes were measured on off-axis Faraday cups, with exit slit widths corresponding to a mass resolution of 2500. The reference materials used to correct for instrumental mass fractionation include magnetite Mg-Charroy, magmatic glass BHVO-2G, magmatic glass CLDR01, spinel group mineral Burma sp, diopside JV1 and olivine ScFa. The magmatic glass CLDR01 was also used as a primary standard to correct for matrix effects. The combined 2SD uncertainties approximate 0.4‰ for $\delta^{18}O$, 0.6‰ for $\delta^{17}O$, and 0.7‰ for $\Delta^{17}O$. All plotted data are calculated as averages of individual SIMS measurements (Tables A.7-8).

3. Results

a. Major and trace element geochemistry

Major and trace element compositions of the selected particles, measured via LA-ICP-MS, are presented in Tables A.1-6. Based on major element geochemistry, individual particles are classified into the 'normal chondritic', 'CAT-like' and 'High Ca-Al' cosmic spherule types, as defined by Cordier et al. (2011). Following this classification, 25 out of the 35 initially selected particles (71%) fall in the 'CAT-like' region of a Fe/Si vs CaO + Al_2O_3 plot (Fig. 1), with most particles displaying Fe/Si ratios below 0.04. However, in this sample set no particles plot in the 'High Ca-Al' region, although Goderis et al. (2020) report a 'High Ca-Al' particle content of 8% amongst the recovered cosmic spherules from Widerøefjellet. While many particles confirm a relatively high combined CaO and Al_2O_3 content (>9 wt.%) used as a selection criterion following SEM-EDS analysis, most particles are associated with low Fe/Si ratios, and hence, these samples plot in the 'CAT-like' region of the plot, rather than in the 'High Ca-Al' region. To avoid any possible extraction or operator bias, the data set obtained is complemented with literature data in the following sections (Cordier et al., 2011; Goderis et al., 2020; Lampe et al., 2021).

The major element classification can be complemented with trace element concentrations and patterns. A plot of the trace element concentrations normalized against the elemental concentrations of CI chondritic values (McDonough & Sun, 1995) provides a visual indication of the relative degree of enrichment or depletion of an element in the various chemical cosmic spherule subgroups (Fig. 3). However, the CI chondrite bulk composition is not necessarily the best reference to a potential starting composition in every individual case, since particles can originate from different parent bodies, but it

has nevertheless proven to be a useful compromise when working with larger, more varied datasets (Frank et al., 2023). In addition, the potential presence of calcium-aluminum-rich inclusions (CAIs) or other refractory phases could strongly influence the bulk composition of individual particles. In the case of large refractory mineral phases, the isotopic composition of oxygen may exhibit extreme values, closer to solar values (Guan et al., 2000). The admixture of smaller CAIs to cosmic spherules can unfortunately not be fully excluded, but CAI-like material is in general not abundant enough (<0.5%) to significantly perturb the bulk compositions of CI chondrites (Frank et al., 2023).

The 'CAT-like' particles (WF18-0502, 0504, 0506, 0221, 0224, 0229, 0231, 0208, 0413, 0416, 0425, 0415, 0227, 0207, and 0419, and WF18-AD1, AD2, AD3, AD4, AD5, AD6, AD7, AD8, AD9, and AD10) appear to be enriched in refractory elements (Zr, Hf, Sc, Al, Y, Ti, Lu, Er, Th, Ho, Tb, Tm, Dy, Gd, U, Nd, Sm, Pr, La, Ta, Nb, and Yb) compared to CI chondrites. In contrast, the (moderately) volatile elements (V, Co, Ni, Fe, Cr, Mn, Na, Zn, Pb) are more strongly depleted in these particles. However, several moderately volatile elements including Ce, Eu, Si, Sr, and Ba display roughly chondritic values, or plot slightly above chondrite. Additionally, deviations of individual 'CAT-like' and 'High Ca-Al' particles than the calculated means can be observed. For example, vitreous particles WF18-0502 and WF18-0504 consistently display higher enrichments in refractory elements (Zr – Yb) relative to the other 'CAT-like' samples. These two glassy 'CAT-like' particles furthermore display Fe/Mn ratios (~50) and Fe/Mg ratios (~0.5 and ~0.7), distinct from all other samples analysed.

All 'CAT-like' samples appear to be enriched in REEs relative to CI chondrite values (Fig. 4). All particles display nearly chondritic values, except for samples WF18-0502 and 0504, which display the highest degree of lanthanide enrichment and progressive enrichment in light REEs. Their REE concentrations range from ~15-fold that in CI chondrite in the case of Tm to ~150-200-fold that in CI chondrite in the case of La. To better quantify these relative enrichments, average REE_N values, which represent the average CI-normalized REE concentrations, can be used. Sample WF18-0502 and 0504 have REE_N values of 48.0 and 54.1, respectively. The REE_N values of the other particles characterized vary between 2.3 (WF18-0208) and 20.9 (WF18-0413). For comparison, the averaged REE_N values within this dataset are 8.9 (±5.1; 1SD) for 'CAT-like' cosmic spherules (excluding samples WF18-0502 and 0504), and 4.0 (±3.3; 1SD) for 'normal chondritic' cosmic spherules. Additionally, various REE anomalies are observed for Ce, Eu and Tm. To quantify these REE anomalies, Ce*, Eu* and Tm* values can be introduced:

$$Ce^* = \frac{Ce}{\sqrt{La \times Nd}} \qquad Eu^* = \frac{Eu}{\sqrt{Sm \times Gd}} \qquad Tm^* = \frac{Tm}{\sqrt{Er \times Yb}}$$

Elements listed in the equations depict their mass fractions normalized to CI chondrite values.

Overall, 14 out of the 25 'CAT-like' samples (56% of the particles studied here) display a Ce* value below 0.7, and therefore can be considered to display a negative Ce anomaly (Braun et al., 1990). Two samples (WF18-0425 and 0207; 8% by number) have Ce* values of respectively 3.9 and 2.1, corresponding to positive Ce anomalies. Nine particles (WF18-0502, 0504, 0506, 0221, 0416, 0415, and 0419, and WF18-AD1 and AD10; 36% by number) display Ce* values between 0.7 and 1.3, indicating the absence of strong Ce anomalies. Both positive and negative Ce-anomalies, observed among the 'CAT-like' sample population in this work, conflict with prior observations of only negative Ce anomalies reported for comparable V-type cosmic spherules (Cordier et al., 2011; Goderis et al., 2020).

Additionally, eight samples (WF18-0502, 0504, 0416, 0425, 0207, and 0419, and WF18-AD3 and AD7; 32% by number) show negative Eu anomalies (Eu* < 0.7), although the anomalies observed are often less extreme than those observed for Ce (Tables A.2,5-6). The two aforementioned particles that display positive Ce anomalies (WF18-0425 and 0207) also show the most pronounced negative Eu anomalies (Eu* values of 0.55 and 0.64, respectively). A single particle (WF18-AD8; 4% by number) has a positive Eu anomaly of 1.9. The remaining sixteen cosmic spherules (64% by number) display no significant Eu anomalies (Eu* = 0.7 – 1.3). Furthermore, a pronounced positive Tm anomaly with Tm* value equal to 1.5 is observed in the case of cosmic spherule WF18-0425. Overall, this particle is uniquely characterized by positive Ce and Tm anomalies and a negative Eu anomaly. Furthermore, (moderately) negative Tm anomalies in the range of 0.3 to 0.7 are observed for five particles (WF18-0221, 0416, and 0415, and WF18-AD1 and AD6). A further investigation of these observed anomalies is elaborated in section 4f.

Variable levels of enrichment in light and heavy REEs (LREEs and HREEs, respectively) are described in literature (Cordier et al., 2011; Soens et al., 2022). To quantify these differences, $(La/Yb)_N$ values are introduced, which represent the ratio of CI-normalized La and Yb concentrations, providing an indication on the degree of tilt in the REE patterns. Of the particles examined here, eleven display a LREE-enriched pattern with $(La/Yb)_N > 1.5$ (WF18-0502, 0504, 0506, 0221, 0416, 0415, 0207, and 0419, as well as WF18-AD2, AD3, and AD10), whereas the remaining 14 particles display a flat REE pattern with $(La/Yb)_N$ in the range of 0.6 to 1.4 (Tables A.2,5-6; Fig. 4).

b. Oxygen isotopic composition

The $\delta^{17}O$, $\delta^{18}O$ and $\Delta^{17}O$ data for 23 of the cosmic spherules studied are summarized in Table A.7. These particles comprise 9 'CAT-like', 10 'normal chondritic' and 4 spherules not analysed by LA-ICP-MS. Texturally, this group of 23 spherules consists of 12 V-type, 3 BO-type, 4 transitional CC/BO-type, 2 Po-type and 2 CC-type particles. Fig. 6A illustrates the linear trend that emerges when plotting $\delta^{17}O$ vs

$\delta^{18}O$ values, with data points plotting parallel to the terrestrial fractionation line (TFL). The $\delta^{18}O$ values of 'normal chondritic' spherules range from 12‰ and 52‰, while the $\delta^{18}O$ values of 'CAT-like' spherules range from 8‰ to 59‰. These values overlap with and extend the range of values previously reported in literature (Cordier et al., 2011: 13‰ > $\delta^{18}O$ of 'normal chondritic' particles > 20‰, 15‰ > $\delta^{18}O$ of 'High Ca-Al' cosmic spherules > 28‰; Taylor et al., 2005: 4‰ > $\delta^{18}O$ > 41‰; Suavet et al., 2010: 9‰ > $\delta^{18}O$ > 43‰; Goderis et al., 2020: 10‰ > $\delta^{18}O$ > 44‰; Lampe et al., 2022; 5‰ > $\delta^{18}O$ > 65‰; Soens et al., 2022: 12‰ > $\delta^{18}O$ > 44‰). No clear trends are observed in the data for both the 'normal chondritic' and 'CAT-like' spherules. However, two of the three spherules with the highest $\delta^{17}O$ and $\delta^{18}O$ values are classified as 'CAT-like'. WF18-0214 displays negative values for both $\delta^{17}O$ and $\delta^{18}O$ ($\delta^{17}O \approx -2.2$‰; $\delta^{18}O \approx -7.0$‰).

The $\Delta^{17}O$ values for 7 particles (WF18-0201, 0207, 0209, 0215, 0221, 0413, and 0419) cannot be distinguished from the TFL given the associated analytical uncertainty (Tables A.7-8). Following mass-dependent fractionation processes and mixing with atmospheric oxygen, the original oxygen isotopic signature of these cosmic spherules and thus, the position of the corresponding data points relative to the TFL remains unknown. All other samples analysed have $\Delta^{17}O$ values that are distinct from the TFL (Fig. 6B). Particles WF18-0204, 0208, 0227, 0501, 0505, 0506, 0512, 0513 and 0514 display negative $\Delta^{17}O$ values down to -3.5‰ (39% by number of all particles; 57% of those that can be classified). Seven particles (WF18-0214, 0403, 0502, 0504, 0507, 0508, and 0509) have a positive $\Delta^{17}O$ value up to +2.3 ‰ (30% of all particles; Fig. 6B).

4. Discussion

As this study concerns particles that are generally considered to have experienced high degrees of vaporization, a significant modification of their chemical compositions is expected as a result of the processes taking place during atmospheric entry. To provide a more informative comparison, the results of this study are plotted together with data from literature (Cordier et al., 2011; Goderis et al., 2020; Lampe et al., 2022). It should be noted that all samples in Cordier et al. (2011) were V-type spherules, whereas the samples in Goderis et al. (2020) and Lampe et al. (2022) comprise of a mixture of various textural and chemical types of cosmic spherules (V-type, BO-type, CC-type, Po-type). Goderis et al. (2020) provide a representative overview on cosmic spherules from Widerøefjellet, the same sampling location as the cosmic spherules described in this work.

a. Effects from parent materials

The oxygen isotopic data provide important clues towards progenitor identification through comparison of $\delta^{18}O$, $\delta^{17}O$ and $\Delta^{17}O$ values with those of the presumed parent bodies (Fig. 6A-B). In a plot of $\delta^{18}O$ vs $\Delta^{17}O$ (Fig. 6B), 14 of the 23 spherules analysed (61%) plot within three groups (*Groups 1*, *2* and *3*) of the original four groups identified by Suavet et al. (2010), and two data points plot in the vicinity of *Group 4* (within 1‰ for $\Delta^{17}O$ and 6‰ for $\delta^{18}O$). Three 'normal chondritic' spherules plot in or near the *Group 1* area, and are considered to originate from CO, CV or CM carbonaceous chondrites (Suavet et al., 2010). Two other 'normal chondritic' spherules plot in the vicinity of *Group 2* (below and to the right of the previously defined field), potentially indicating a CR carbonaceous chondritic origin. Two additional 'normal chondritic' spherules plot to the right of *Groups 1* and *2*, likely also derived from a carbonaceous precursor. In contrast, the three 'normal chondritic' spherules that plot above the TFL likely derive from ordinary chondritic precursors. Thus, of the 10 'normal chondritic' particles that could be classified (125-400 µm size fraction), 30% derive from OC and 70% derive from CC. These percentages are in reasonable agreement with those reported in literature (40% OC and 60% CC out of 5 'normal chondritic' spherules in the 443-760 µm size fraction; Cordier et al., 2011). Although this concerns a limited number of particles only, it may still suggest a similar population of parent body materials among the highly vaporized particles, which would indicate that they derive from comparable solar system reservoirs. As for the nine 'CAT-like' spherules, the deviations from the TFL are generally less pronounced. Two 'CAT-like' spherules (samples WF18-0502 and 0504; ~22% by number) may originate from achondritic precursor bodies (see next paragraph). Of the remaining seven 'CAT-like' spherules, three spherules lie too close to the TFL to allow precursor identification (~33%) (Fig. 6B). Of the remaining four, three spherules are likely of carbonaceous chondritic origin (~75%) and a single spherule appears to be derived from an ordinary chondritic precursor (~25%), in line with the observations for "normal chondritic" spherules.

The elemental composition of the samples analysed provides additional clues about their parentage. Most samples, except for WF18-0502 and 0504, display REE trends that hint towards chondritic compositions and thus precursor materials. However, samples WF18-0502 and WF18-0504, which show distinct, heavily enriched REE patterns (Fig. 4), are likely derived from achondritic objects or precursor bodies (Soens et al., 2022). This is further strengthened by their distinct positions in the Fe/Mg vs Fe/Mn diagram (Fig. 7), which hint towards a lunar, Martian or Vestian origin. In general, achondritic cosmic spherules have high CaO and/or Al_2O_3 contents and display highly enriched REE patterns (Cordier et al., 2012; Soens et al. 2022). In addition, as chondritic materials are on average more Mg-rich than achondritic materials (Cordier et al., 2012), and since Mg-rich (mafic) minerals (e.g., enstatite and forsterite) have relatively high melting temperatures, achondritic particles may potentially melt more easily than chondritic particles (Cordier et al. 2012; Genge, 2017). As a result,

achondritic particles are more prone to lead to the formation of V-type textures, as displayed by particles WF18-0502 and 0504. In addition, the fusion crusts of achondrites are generally more glassy than the fusion crusts of chondrites (Genge & Grady, 1999). Genge (2017) also found that the disappearance of individual mineral phases in an eucrite particle during melting follows the order olivine, spinel, plagioclase, and finally clinopyroxene. Based on the oxygen isotope ratio data collected in this work, in combination with a literature survey, "normal chondritic", 'CAT-like', and 'High Ca-Al' spherules largely derive from the same parent body reservoirs, implying that atmospheric processes affected these particles differently.

b. Influence of mineral constituents

The identified petrographic types of the spherules studied are listed in Table 1. Fig. 2 provides an overview of the various textural types identified in this study. The influence of mineralogical components on the final observed composition can be unravelled based on various geochemical plots. Fig. 8 summarizes the atomic Si/Al vs Mg/Al ratios for a set of normal chondritic, CAT-like, and 'High Ca-Al' particles. This diagram has been used to illustrate the influence of Mg-rich pyroxene and olivine on the bulk chemistry of cosmic spherules. Among the 'normal chondritic' cosmic spherules characterized by Cordier et al. (2011), Goderis et al. (2020), and this work, various particles plotting along mixing lines in the direction of enstatite and forsterite are identified. This is rarely the case for 'CAT-like' or 'High Ca-Al' particles, likely the result of evaporation processes driving the compositions to the origin of this binary plot. Although limited in number, several 'High Ca-Al' particles still follow the enstatite admixture line, while a small number of 'CAT-like' particles plot in the direction of the forsterite field (Fig. 8). This observation may support the occurrence of a mineralogical influence on the final composition of cosmic spherules.

Such effect is further demonstrated in Fig. 9, where most 'normal chondritic' particles plot near the origin of a diagram plotting atomic Al/Si vs Ca/Si, in proximity of the low-Ca pyroxene field. In contrast, both 'CAT-like' and 'High Ca-Al' spherules plot away from the origin, to some degree reflecting evaporation processing that affected the atomic Ca/Si (and Al/Si) ratios. Nevertheless, a significant number of 'CAT-like' and 'High Ca-Al' spherules plot close to the low-Ca plagioclase field, while one 'High Ca-Al' particle plots in proximity of the high-Ca plagioclase field, and a single 'CAT-like' particle overlaps with the high-Ca pyroxene field. This observation suggests that these particles were likely dominated by a single mineral phase, and had primary mineralogies rich in Al and Ca in the first place. The predominance of a plagioclase component in this particle is confirmed based on the occurrence of a positive Eu anomaly in the bulk REE pattern (Fig. 4).

The five classes of REE patterns identified in Section 3a (Fig. 5A-E) cover the 25 'CAT-like' cosmic spherules identified in this study. However, between the REE patterns of these 25 particles, 9 patterns display a comparable pattern that was not observed in Goderis et al. (2020), where enhanced Pr, Nd, and Sm enrichments give rise to a more bulging, curved appearance of the respective REE trend in the LREE region, characterized by $(La/Pr)_N < 0.7$ (Fig. 5F). Cordier et al. (2011) also did not report these bulging patterns among their particle set. Besides a potential deviating starting composition, Pr, Nd and Sm have slightly lower condensation temperatures (50% T_C = 1582, 1602 and 1590 K, respectively; Lodders, 2003) than HREEs (50% T_C = 1659 K for Gd–Tm; Lodders, 2003), which might indicate that these 'CAT-like' particles experienced peak temperatures, presumably slightly above 1600 K, allowing for (mild) fractionation of Pr, Nd and Sm from the HREEs.

Finally, a diagram of Sm/Nd vs Lu/Hf can be used to highlight the potential presence of phosphates in cosmic spherules (Fig. 10). Most 'normal chondritic' particles plot within a narrow range of Lu/Hf, showing stronger variation in Sm/Nd. Melting and fractional crystallisation are known to heavily fractionate Sm/Nd, while the Lu/Hf ratio is somewhat less affected (Ali et al., 2016). In contrast, meteoritic phosphate usually has a distinct Lu/Hf ratio due to the incompatibility of Hf in phosphate (Chernonozhkin et al. 2021). Consequently, in some cases, a Lu/Hf ratio deviating from the chondritic field may indicate the presence of phosphate in the precursor fragments leading to the formation of micrometeoroids. Such deviations are mostly observed for 'CAT-like' particles, and perhaps a singular 'High Ca-Al' spherule (Fig. 10). Combined with the other findings in this section on mineral constituents, these observations indicate the influence of mineralogy on the final chemical composition of cosmic spherules, in which the contribution of particular minerals (including plagioclase, high-Ca pyroxene, and possibly phosphate and CAIs) may preferentially lead to the formation of 'CAT-like' and 'High Ca-Al' cosmic spherules.

c. Alteration and chemical weathering under Antarctic conditions

The effects of chemical weathering include the removal of primary mineral phases, such as olivine and glass, and incrustations by weathering products, such as Al-rich clays (van Ginneken et al., 2016). The formation of clays, and the accompanying increased levels of Al, induce a chemical shift of the particles towards the 'High Ca-Al' and 'CAT-like' fields. In addition, ferrihydrite and jarosite – of which the formation leads to increased Fe contents – have been shown to precipitate within cavities of micrometeorites from the Transantarctic Mountains (TAM), resulting in pseudomorphic textures within heavily altered particles (van Ginneken et al., 2016). Sulfate in sea sprays promotes the formation of jarosite, which may in turn explain the low presence of jarosite outside of the TAM

collection, since the Widerøefjellet sampling site is quite far from the coast (>200 km). Glass is known to alter into palagonite gels with sequential replacement indicative of varying water-to-rock ratios. Metal may be replaced by Fe-oxides/hydroxides (including goethite, lepidocrocite, and maghemite), which leads to a globally lower Fe content. However, magnetite formed during atmospheric entry is generally resistant to alteration by interaction with the terrestrial environment (van Ginneken et al., 2016). Based on these observations, alteration and chemical weathering may lead to passive enrichment and phase transformation that may subsequently lead to changes in the bulk chemical composition, which may in turn (partially) lead to assignment to the 'High Ca-Al' or 'CAT-like' chemical groups. In this dataset, a total of 64% (9 out of 14) of the 'CAT-like' spherules that were assigned a level of weathering (Table 1; van Ginneken et al., 2016) have a weathering level of either 0a or 1a, while this is the case for 80% (8 out of 10) of the 'normal chondritic' spherules. Thus, chemical weathering effects, passive terrestrial enrichments and phase transformations may have played a minor role here.

d. Atmospheric alteration processes: evaporation and metal bead extraction

The Fe/Si vs CaO + Al_2O_3 diagram (Fig. 1) allows comparison of the bulk composition of cosmic spherules of various sampling locations and textural types (Cordier et al., 2011; Goderis et al. 2020; Lampe et al. 2022). No 'High Ca-Al' samples were identified in this study; 10 of the samples characterized in this work plot in the 'normal chondritic' region (~29%), and 25 samples plot in the 'CAT-like' region (~71%). This contrasts the results of Cordier et al. (2011), who reported 165 'normal chondritic' (~88%), 3 'CAT-like' (~2%), and 19 'High Ca-Al' (~10%) particles. Similarly, Goderis et al. (2020) plotted 39 samples (~80%) as 'normal chondritic', 6 samples as 'CAT-like' (~12%), and 4 samples as 'High Ca-Al' (~8%). The TAM particles of Cordier et al. (2011) appears to contain a considerably smaller fraction 'CAT-like' cosmic spherules relative to the SRM collection. Although the number of particles studied here is limited, the distribution among chemical groups may be linked to a sampling bias or the limited value of color as a discriminator for high degrees of evaporation. Alternatively, the highly variable 'CAT-like'/'High Ca-Al' spherule abundance might be related to the sampling locations, with distinct environmental conditions in the Victoria Land Transantarctic Mountains and the Sør Rondane Mountains (Rochette et al., 2008; Goderis et al., 2020). Indeed, the sampling location, and in particular the distance to the ocean, may potentially introduce bias in the micrometeorite collections through distinct weathering or alteration processes (e.g., whether or not jarosite is formed; Baccolo et al., 2021, van Ginneken et al., 2016), giving rise to micrometeorite populations specific to particular sampling sites. The difference observed may also be linked to the textural type, as Cordier et al. (2011) solely studied glass cosmic spherules, rather than a mixture of petrographic types of cosmic spherules, as done in Goderis et al. (2020). Combining various petrographic types of cosmic sphe rules also results

in more scatter in the data of the 'normal chondritic' region. For example, BO-type cosmic spherules generally display higher Fe contents relative to glass spherules, plotting more towards the right side of the Fe/Si vs CaO + Al_2O_3 diagram (Fig. 1).

In a diagram of Fe/Mg vs Fe/Mn (Fig. 7), the 'normal chondritic' particles of Cordier et al. (2011) and Goderis et al. (2020) generally plot in the chondritic range, which contrasts most 'CAT-like' spherules characterized in this study, as these are shifted towards the left edge of the plot. However, this trend does not necessarily imply that these spherules do not derive from a chondritic precursor; processes such as metal bead formation and subsequent ejection can also lead to lower Fe/Mg ratios, whereas Fe/Mn ratios would only vary to a more moderate extent. When comparing the Mg/Al vs. Si/Al values of this study with literature data (Fig. 8), the 'normal chondritic' cosmic spherules plot close to the CC or OC fields, or moderately in the direction of the mineral constituents enstatite or forsterite. However, a considerable fraction (36% by number) of the 'CAT-like' spherules studied here, appear to plot along the modelled evaporation trajectories (from the CC and OC fields), towards lower Si/Al and Mg/Al values, with a wide range in the degree of evaporation (50–90%) (Fig. 8). In contrast, a different population of the 'CAT-like' particles from this study (40%) does not follow this evaporation trend and displays low Mg/Al ratios (< 1) at variable Si/Al values (between 2 and 8), plotting towards the left edge of the diagram. Based on the observed Fe/Mg ratios of the 'CAT-like' spherules, these low (< 1) Mg/Al ratios result from high, superchondritic Al contents. An elevated Al concentration likely derives from evaporation effects (Fig. 3) in combination with precursor mineralogy and alteration (Section 4c). In turn, the variations in Si/Al ratios observed for low (<1) Mg/Al ratios imply the occurrence of metal bead extraction, as the effects of metal bead formation on the bulk spherule composition are considerably larger than the effects of evaporation only. This is confirmed by studies of Fe isotope ratios that confirm metal bead ejection (Lampe et al., 2022) and the occurrence of metal beads in several of the cosmic spherules (Fig. 2).

Combining all data acquired provides additional clues on the processes experienced by the cosmic spherules studied in this work. For instance, cosmic spherules with the lowest atomic Fe/Si ratios also display the widest range of $\delta^{18}O$ values, ranging from 8 to 59‰, whereas high $\delta^{18}O$ values (>30‰) are only observed for particles with low atomic Fe/Si ratios (<0.15). Two main processes can be invoked to explain this trend. The atomic Fe/Si ratio at the bulk level of the particle as a whole decreases upon metal bead ejection, whilst this remaining residual phase itself might be more prone to isotopic fractionation due to evaporation, explaining the wide range of $\delta^{18}O$ values (Lampe et al., 2022). This observed trend might be an illustration that the processes of metal bead extraction and isotopic fractionation do not necessarily occur independently. Measurements of Fe isotope ratios in micrometeorites (Alexander et al., 2002; Taylor et al., 2005; Lampe et al., 2022) have shown how metal

bead formation and free evaporation control the final Fe concentrations and $\delta^{56}Fe$ and $\delta^{57}Fe$ values. Here, two theoretical pathways are possible (cfr. Taylor et al., 2005); (i) early evaporation of the main phase, followed by late metal bead segregation, or (ii) early metal bead extraction, followed by late evaporation of the residual material. These are two extreme scenarios, with many intermediate options possible. Analogous to these studies, Fe loss and the increase of $\delta^{18}O$ (similarly to $\delta^{57}Fe$) via various pathways might have occurred for the dataset presented.

The influence of evaporation can also be traced using a Sc + Y + Zr + Hf vs $CaO + Al_2O_3$ diagram (Fig. 11). The sum of CaO and Al_2O_3 mass fractions represents the content of refractory lithophile major elements, which can also be affected by mineralogy, while Sc, Y, Zr and Hf are four of the most refractory lithophile trace elements (Fig. 3), and their cumulative concentration can be used to trace evaporative processes. In general, chondritic parent bodies have been reported to have a combined Sc, Y, Zr and Hf concentration in the range of 10 to 18 µg/g, with a combined Sc + Y + Zr + Hf content of 11.4 µg/g for Ivuna-type (CI) chondrites (Sanloup et al., 2000; Braukmüller et al., 2018; McDonough & Sun, 1995).

Based on a comparison to the CI chondrite values, plotted as a line with a CI chondritic proportion of $CaO + Al_2O_3$ and Sc + Y + Zr + Hf based on McDonough & Sun (1995), particles can be discriminated based on their position above or below this line. Compared to literature data, the 'CAT-like' samples from this study generally plot closer towards the upper right corner of the diagram, illustrating their more evaporated nature. Additionally, the trend lines observed for these 'CAT-like' particles indicate that the relative Sc + Y + Zr + Hf enrichments are higher than those of $CaO + Al_2O_3$, which is consistent with the difference in their condensation temperatures (50% T_C = 1659 – 1741 K and 1517 – 1653 K, respectively; Lodders, 2003), thus, elemental fractionation of Ca from these refractory elements may have occurred in strongly evaporated particles. Alternatively, this could imply the prevalence of incompatible trace element enriched mineral phases, or an originally lower abundance of minerals rich in Ca and Al. The deviations of the 'normal chondritic' samples of this study can be analogously explained, albeit these are less pronounced than the deviations of the 'CAT-like' samples. These 'normal chondritic' spherule data generally do not deviate much from the 'normal chondritic' spherule data of Cordier et al. (2011) and Goderis et al. (2020). Finally, 'High Ca-Al' data from these studies also clearly display deviations, but these are still less pronounced than those of the 'CAT-like' data from the present study.

e. Quantifying evaporative losses

Using the cumulative CaO + Al_2O_3 and Sc + Y + Zr + Hf mass fractions, the degree of evaporation (DoE) based on refractory lithophile trace elements can be calculated, allowing for a comparison between different cosmic spherules and studies:

$$DoE_{ScYZrHf} = 1 - \frac{Sc + Y + Zr + Hf\ (CI\ chondrites)}{Sc + Y + Zr + Hf\ (cosmic\ spherule)}$$

This gives rise to spherules with two to four times the Sc + Y + Zr + Hf content of CI chondrites, corresponding to 50% and 75% evaporation, respectively. As such, the 25 'CAT'-like spherules of this study show $DoE_{ScYZrHf}$ between 52% and 97%, with 10 spherules (40%) showing degrees of evaporation of 90% or more. For the 'normal chondritic' spherules, the calculated degrees of evaporation range between 37% and 84%, with 8 of the 10 spherules (80%) falling below a degree of evaporation of 70%. This illustrates the generally higher evaporated nature of 'CAT-like' spherules, assuming a comparable starting composition.

To better constrain the extent of evaporative losses in the studied particles, other parameters can be proposed as well to form the basis of a novel DoE definition. Next to enrichments of Sc + Y + Zr + Hf, this DoE can also be based on CaO + Al_2O_3 + TiO_2 contents (oxide%) and Mg/Al ratios (atomic). These alternative DoEs can be defined as follows:

$$DoE_{Mg/Al} = 1 - \frac{Mg/Al\ (cosmic\ spherule)}{Mg/Al\ (CI\ chondrites)}$$

$$DoE_{AlCaTi} = 1 - \frac{Al_2O_3 + CaO + TiO_2\ (CI\ chondrites)}{Al_2O_3 + CaO + TiO_2\ (cosmic\ spherule)}$$

The DoEs of the 'CAT-like' spherules studied based on Mg/Al ratios are consistent; 23 out of 25 'CAT-like' spherules (92%) were evaporated by more than 50%. Most 'normal chondritic' spherules, however, plot in the vicinity of chondritic fields, illustrating their less evaporated nature. In addition, a DoE based on $^{18}O/^{16}O$ ratios can also be introduced, based on the Rayleigh fractionation law. The $^{18}O/^{16}O$-based DoE values can be calculated as follows:

$$DoE\,{}^{18}O/{}^{16}O = \left({}^{R}/_{R_0}\right)^{-\frac{1}{(\alpha-1)}}$$

Here, R is the $^{18}O/^{16}O$ ratio of the cosmic spherule, R_0 is the $^{18}O/^{16}O$ ratio of a hypothetical parent body (in this case 0.002015, corresponding to a $\delta^{18}O$ value of 5‰), and α is the isotopic fractionation factor (1.0237; Wang et al., 2001). In Table 1, the DoEs, based on different criteria, are listed and compared. Albeit there is a moderate to fair correlation between the DoEs calculated based on elemental proxies (Pearson's correlation coefficients of $r_{ScYZrHf,\ AlCaTi}$ = 0.789; $r_{ScYZrHf,\ Mg/Al}$ = 0.739; $r_{AlCaTi,\ Mg/Al}$ = 0.834), the DoEs based on elemental proxies generally have a very weak to nearly no correlation with the DoE based on $^{18}O/^{16}O$ ratios (Pearson's correlation coefficients $r_{ScYZrHf,\ \delta18O}$ = 0.287; $r_{AlCaTi,\ \delta18O}$ = 0.323; $r_{Mg/Al,}$

$_{\delta 18O}$ = 0.471). The correlations of DoEs calculated based on element compositions with the average REE_N (excluding achondritic particles WF18-0502 and 0504) are moderately weak (Pearson's correlation coefficients $r_{ScYZrHf,\ REE}$ = 0.699; $r_{AlCaTi,\ REE}$ = 0.543; $r_{Mg/Al,\ REE}$ = 0.666), and the DoEs calculated based on $^{18}O/^{16}O$ ratios show no correlation with the DoEs based on the average REE_N (Pearson's correlation coefficient of 0.104). This observation hints towards a complex pattern of processes influencing the final oxygen isotopic and chemical compositions of cosmic spherules. Likely the final oxygen signature is affected by mixing with atmospheric oxygen during the atmospheric passage and with Antarctic ice more significantly than can be anticipated and deconvoluted.

Upon comparing the average DoEs for the whole 'CAT-like' and 'normal chondritic' sample subsets, it is clear that the 'CAT-like' particles are more highly evaporated than the 'normal chondritic' particles. This is illustrated by higher average AlCaTi-based DoEs (0.80 vs 0.39), ScYZrHf-based DoEs (0.84 vs 0.63), and Mg/Al-based DoEs (0.79 vs 0.29). This is also the case for the averages of the $^{18}O/^{16}O$-based DoEs (0.56 vs 0.43). When investigating $^{18}O/^{16}O$-based DoEs of 'High Ca-Al' data from literature (Cordier et al., 2011), the 'High Ca-Al' particles surprisingly appear slightly less evaporated than 'normal chondritic' particles (0.57 vs 0.65).

Upon investigating the calculated DoE values of the particles that were previously discussed to be likely dominated by a single mineral phase, and presumably had primary mineralogies rich in Al and Ca (cfr. Section 4b & Fig. 9), it was also found that these values are generally lower than those of most other particles. This further illustrates their less evaporated nature (cfr. Fig. 11).

f. Redox effects

The CI-normalized elemental ratios of the 'CAT-like' and 'normal chondritic' samples characterized in this work are compared with literature data in Fig. 3. The 'CAT-like' samples from this study clearly plot higher than those reported in literature (Cordier et al., 2011; Goderis et al., 2020). From Zr up to Yb, 'CAT-like' are ~10-fold times more enriched than CI chondrites, whereas 'normal chondritic' are ~3-fold times more enriched than CI chondrites. This trend appears less pronounced for elements more volatile than Yb (V until Pb; Lodders et al., 2003). These clues for evaporation processes are further strengthened by the REE patterns (cfr. Fig. 4), where the Ce and Eu enrichments are deemed to result from the variety of oxidation states that these elements can attain. Contrary to most lanthanides, which have a strong preference for the +III oxidation state, Ce and Eu can also have stable oxidation states of +IV and +II, respectively (Trail et al., 2012). This wider variety of stable oxidation states makes both elements more prone to elemental fractionation, which can – besides precursor mineralogy –

partly explain the Ce and Eu anomalies in the lanthanide patterns of the cosmic spherules studied (Cordier et al., 2011, Trail et al., 2012).

Eight samples show mildly negative Eu anomalies (0.5 – 0.7), which are commonly observed in cosmic spherule studies (Cordier et al., 2011; Goderis et al., 2020). Negative Eu anomalies can be caused by the crystallisation of plagioclase, which preferentially takes up Eu upon crystallisation, which in turn is linked to the stable +II state of Eu (see section 3a). This recrystallisation is a pre-atmospheric effect, which relates to the crystallisation of plagioclase in the precursor body. Besides the observed Ce and Eu anomalies, a Tm anomaly (Tm* = 1.5) for sample WF18-0425 was observed as well. Thulium anomalies in extraterrestrial materials have been reported in literature (Dauphas & Pourmand, 2015), but not observed yet for cosmic spherules. While Ce and Eu anomalies can be explained by the crystallisation of specific mineral phases and the existence of highly stable additional oxidation states of Ce and Eu, the origin of the positive Tm anomaly is more challenging to constrain. A possible explanation for this anomaly is the potential presence of CAIs in this particular cosmic spherule, as certain types of CAI are enriched in Tm (e.g., Type II CAI) (Conard, 1976; Kornacky & Fegley, 1986). The positive Tm anomaly can result from early solar nebula processes, or from the nature of the bulk parent body, with a larger relative contribution of CAIs admixed to a chondritic matrix, for example a CV-type carbonaceous chondrite. The positive Tm anomaly of sample WF18-0425 is paired with a positive Ce anomaly (Ce* = 3.9) and a negative Eu anomaly (Eu* = 0.5).

As a final note, the classification scheme proposed by Cordier et al. (2011) has proven to be an efficient system when investigating major and trace elements, even beyond V-type cosmic spherules. However, it is not entirely compatible with interpretations made solely based on oxygen isotopic data. While Cordier et al. (2011) suggests that 'High Ca-Al' cosmic spherules display a higher degree of evaporation than 'CAT-like' cosmic spherules, neither the 'CAT-like' nor the 'normal chondritic' spherules (no 'High Ca-Al' specimen were encountered in the sample subset studied) comprise a restricted interval in $\delta^{18}O$ vs $\delta^{17}O$ diagrams, but rather display widely overlapping ranges along the terrestrial fractionation line (TFL). This observation confirms that a wide array of processes influences the final chemical and oxygen isotopic composition of cosmic spherules. As the particles studied also reflect a large variety of parent bodies and processes that affect the elemental and oxygen isotopic composition, the construction of a single unambiguous classification scheme that comprises all highly vaporized cosmic spherules studied, taking into account their respective textural features, elemental compositions and oxygen isotopic compositions, remains challenging.

5. Conclusions

Based on their major and trace element composition, the degree of chemical fractionation experienced by the selected particles collected from Widerøefjellet (Sør Rondane Mountains, East Antarctica) – in part caused by atmospheric entry heating – is more pronounced for the highly vaporized cosmic spherules than for other chemical types of cosmic spherules described in literature (Cordier et al., 2011; Goderis et al., 2020). However, the degrees of evaporation experienced by spherules identified as 'CAT-like' type based on the defined set of chemical criteria do not appear to be consistent. As such, this work confirms the existence of a subset of cosmic spherules that is characterised by anomalously high degrees of evaporation (REE_N > 10 for 11 out of 35 studied spherules; 31%). The presumed high degrees of evaporation resulting from exposure to high peak temperatures (> 1500 K) are often supported by high $\delta^{18}O$ values, anomalously high enrichments in refractory elements (e.g., Al, Ti, Y, Zr and Hf), and highly enriched REE patterns. Based on the global trends observed in this work, elemental and isotopic fractionation co-occurs in certain cases but is mostly decoupled in other, most likely as a result of the effects of starting mineralogy, and mixing of the oxygen isotopic signatures with those of the atmosphere and Antarctic ice. In general, the 'CAT-like' cosmic spherules studied reflect a wide variety of processes (evaporation, metal bead ejection, isotopic fractionation, and redox shifts) and precursor materials (ordinary chondrites, carbonaceous chondrites, achondrites). A set of specific precursor minerals (including high Ca pyroxene, plagioclase, and phosphate) is identified that can potentially lead to the 'CAT-like' or 'High Ca-Al' chemical subgroups of cosmic spherules, superimposed by passive enrichment taking place during evaporation. In addition, the significant occurrence of Tm anomalies were observed for the first time in micrometeorites, linking them to CAIs and early solar nebula processes. Finally, the proportions of chemical groups vary among different micrometeorite collections and textural types, implying the potential influence of sampling bias, textural associations and distinct alteration effects.

6. Acknowledgements

SG and PC acknowledge funding by the Research Foundation – Flanders (FWO-Vlaanderen), and the VUB strategic program for instrument purchase and support. SG, PC, SMCh and FV acknowledge support from the EoS project ''ET-HoME". SG and PC thank the Belgian Science Policy (BELSPO) for support through different projects (BELAM, Amundsen, BAMM!, and DESIRED). FVM thanks the Research Foundation Flanders (FWO) for funding this PhD research (research project 11C2520N). Warm thanks go to the CRPG in Nancy for the use of their SIMS instrument, and the SURF department of the VUB for the use of their SEM-EDS instrument.

7. References

Alexander, C. M. O'D., Taylor, S., Delaney, J. S., Ma, P. and Herzog, G. F. 2002. Mass-dependent fractionation of Mg, Si and Fe isotopes in five stony cosmic spherules. *Geochimica et Cosmochimica Acta* 66(1): 173–83.

Ali, K. A., Zoheir, B. A., Stern, R. J., Andresen, A., Whitehouse, M. J. and Bishara, W. W. 2016. Lu–Hf and O isotopic compositions on single zircons from the North Eastern Desert of Egypt, Arabian–Nubian Shield: Implications for crustal evolution. *Gondwana Research* 32: 181–92.

Baccolo, G., Delmonte, B., Niles, P. B., Cibin, G., Di Stefano, E., Hampai, D., Keller, L., Maggi, V., Marcelli, A., Michalski, J., Snead, C. and Frezzotti, M. 2021. Jarosite formation in deep Antarctic ice provides a window into acidic, water-limited weathering on Mars. *Nature communications* 12(1): 1–8.

Barrat, J., Yamaguchi, A., Greenwood, R. C., Bohn, M., Cotton, J., Benoit, M. and Franchi, I. A. 2007. The Stannern trend eucrites: Contamination of main group eucritic magmas by crustal partial melts. *Geochimica et Cosmochimica Acta* 71: 4108–24.

Blanchard, M. B., Brownlee, D. E., Bunch, T. E., Hodge, P. W. and Kyte, F. T. 1980. Meteoroid ablation spheres from deep sea sediments. *Earth and Planetary Science Letters* 46: 178–90.

Braukmüller, N., Wombacher, F., Hezel, D. C., Escoube, R. and Münker, C. 2018. The chemical composition of carbonaceous chondrites: Implications for volatile element depletion, complementarity and alteration. *Geochimica et Cosmochimica Acta* 239: 17–48.

Braun, J. J., Pagel, M., Muller, J. P., Bilong, P., Michard, A. and Guillet, B. 1990. Cerium anomalies in lateritic profiles. *Geochimica et Cosmochimica Acta* 54(3): 781–95.

Brearley, A. J. and Jones, R. H. 1998. Chondritic meteorites. In *Planetary materials*, vol. 36, edited by Papike J. J., 1–191. Washington, D.C.: Mineralogical Society of America.

Chernonozhkin, S. M., McKibbin, S. J., Goderis, S., Van Malderen, S. J., Claeys, P. and Vanhaecke, F. 2021. New constraints on the formation of main group pallasites derived from in situ trace element analysis and 2D mapping of olivine and phosphate. *Chemical Geology* 562: 119996.

Clayton, R. N., Mayeda, T. K., Olsen, E. J. and Goswami, J. N. 1991. Oxygen isotope studies of ordinary chondrites. *Geochimica et Cosmochimica Acta* 55: 2317–37.

Clayton, R. N. and Mayeda, T. K. 1999. Oxygen isotope studies of carbonaceous chondrites. *Geochimica et Cosmochimica Acta* 63: 2089–104.

Conard, R. 1976. A study of the chemical composition of Ca-Al-rich inclusions from the Allende meteorite. Master thesis, Oregon State University. https://ir.library.oregonstate.edu/downloads/qr46r360b.

Cordier, C., Folco, L., Suavet, C., Sonzogni; C. and Rochette, P. 2011. Major, trace element and oxygen isotope study of glass cosmic spherules of chondritic composition: the record of their source material and atmospheric entry heating. *Geochimica et Cosmochimica Acta* 75: 5203–18.

Cordier, C., Suavet, C., Folco, L., Rochette, P. and Sonzogni, C. 2012. HED-like cosmic spherules from the Transantarctic Mountains, Antarctica: Major and trace element abundances and oxygen isotopic compositions. *Geochimica et Cosmochimica Acta* 77: 515–29.

Cordier, C. and Folco, L. 2014. Oxygen isotopes in cosmic spherules and the composition of the near Earth interplanetary dust complex. *Geochimica et Cosmochimica Acta* 146: 18–26.

Das Gupta, R., Banerjee, A., Goderis, S., Claeys, P., Vanhaecke, F. and Chakrabarti, R. 2017. Evidence for a chondritic impactor, evaporation-condensation effects and melting of the Precambrian basement beneath the 'target' Deccan basalts at Lomar crater, India. *Geochimica et Cosmochimica Acta* 215: 51–75.

Dauphas, N. and Pourmand, A. 2015. Thulium anomalies and rare earth element patterns in meteorites and Earth: Nebular fractionation and the nugget effect. *Geochimica et Cosmochimica Acta* 163: 234–61.

Engrand, C., McKeegan, K. D., Leshin, L. A., Herzog, G. F., Schnabel, C., Nyquist, L. E. and Brownlee, D. E. 2005. Isotopic compositions of oxygen, iron, chromium and nickel in cosmic spherules: Toward a better comprehension of atmospheric entry heating effects. *Geochimica et Cosmochimica Acta* 69: 5365–85.

Folco, L. and Cordier, C. 2015. Micrometeorites. *European Mineralogical Union Notes in Planetary Mineralogy* 15: 253–97.

Frank, D. R., Huss, G. R., Zolensky, M. E., Nagashima, K. and Le, L. 2023. Calcium-aluminum-rich inclusion found in the Ivuna CI chondrite: Are CI chondrites a good proxy for the bulk composition of the solar system?. *Meteoritics & Planetary Science* 58(10): 1495–511.

Genge, M. J., Grady, M. M. and Hutchison, R. 1997. The textures and compositions of fine-grained Antarctic micrometeorites— Implications for comparisons with meteorites. *Geochimica et Cosmochimica Acta* 61: 5149–62.

Genge, M. J. and Grady, M. M. 1999. The fusion crusts of stony meteorites: Implications for the atmospheric reprocessing of extraterrestrial materials. *Meteoritics & Planetary Science* 34(3): 341–56.

Genge, M. J., Gileski, A. and Grady, M. M. 2005. Chondrules in Antarctic micrometeorites. *Meteoritics & Planetary Science* 40(2): 225–38.

Genge, M. J. 2006. Igneous rims on micrometeorites. *Geochimica et Cosmochimica Acta* 70(10): 2603–21.

Genge, M. J., Engrand, C., Gounelle, M. and Taylor, S. 2008. The classification of micrometeorites. *Meteoritics & Planetary Science* 43: 497–515.

Genge, M. J., Davies, B., Suttle, M. D., van Ginneken, M. and Tomkins, A. G. 2017. The mineralogy and petrology of I-type cosmic spherules: Implications for their sources, origins and identification in sedimentary rocks. *Geochimica et Cosmochimica Acta* 218: 167–200.

Goderis, S., Soens, B., Huber, M. S., McKibbin, S., Van Ginneken, M., Van Maldeghem, F., Debaille, V., Greenwood, R. C., Franchi, I. A., Cnudde, V., Van Malderen, S., Vanhaecke, F., Koeberl, C., Topa, D. and Claeys, P. 2020. Cosmic spherules from Widerøefjellet, Sør Rondane Mountains (East Antarctica). *Geochimica et Cosmochimica Acta* 270: 112–43.

Guan, Y., McKeegan, K. D. and MacPherson, G. J. 2000. Oxygen isotopes in calcium–aluminum-rich inclusions from enstatite chondrites: new evidence for a single CAI source in the solar nebula. *Earth and Planetary Science Letters* 181(3): 271-7.

Imae, N., Debaille, V., Akada, Y., Debouge, W., Goderis, S., Hublet, G., Mikouchi, T., Van Roosbroek, N., Yamaguchi, A., Zekollari, H., Claeys, P. and Kojima, H. 2015. Report of the JARE-54 and BELARE 2012–2013 joint expedition to collect meteorites on the Nansen Ice Field, Antarctica. *Antarctic Record* 59: 38–72.

Kimura, M., El Goresy, A., Palme, H. and Zinner, E. 1993. Ca-, Al-rich inclusions in the unique chondrite ALH85085: Petrology, chemistry and isotopic compositions. *Geochimica et Cosmochimica Acta* 57(10): 2329–59.

Kitts, K. and Lodders, K. 1998. Survey and evaluation of eucrite bulk compositions. *Meteoritics & Planetary Science* 33(S4): A197–A213.

Kornacki, A. S. and Fegley Jr, B. 1986. The abundance and relative volatility of refractory trace elements in Allende Ca, Al-rich inclusions: implications for chemical and physical processes in the solar nebula. *Earth and Planetary Science Letters* 79(3-4): 217–34.

Kurat, G., Koeberl, C., Presper, T., Franz, B. and Maurette, M. 1994. Petrology and geochemistry of Antarctic micrometeorites. *Geochimica et Cosmochimica Acta* 58: 3879–904.

Lampe, S., Soens, B., Chernonozhkin, S. M., González de Vega, C., van Ginneken, M., Van Maldeghem, F., Vanhaecke, F., Glass, B. P., Franchi, I. A., Terryn, H., Debaille, V., Claeys, P. and Goderis, S. 2022. Decoupling of chemical and isotope fractionation processes during atmospheric heating of micrometeorites. *Geochimica et Cosmochimica Acta* 324: 221–39.

Lodders, K. 2003. Solar system abundances and condensation temperatures of the elements. *The Astrophysical Journal* 591(2): 1220–47.

Love, S. G. and Brownlee, D. E. 1991. Heating and thermal transformation of micrometeoroids entering the Earth's atmosphere. *Icarus* 89: 23–46.

Love, S. G. and Brownlee, D. E. 1993. A direct measurement of the terrestrial mass accretion rate of cosmic dust. *Science* 262(5133): 550–3.

Maurette, M., Immel, G., Hammer, C., Harvey, R., Kurat, G. and Taylor, S. 1994. Collection and curation of IDP's from the Greenland and Antarctic ice sheets. *Analysis of Interplanetary Dust Conference Proceedings* 310(1): 277–90. Houston: American Institute of Physics.

McDonough, W. F. and Sun, S. S. 1995. The composition of the Earth. *Chemical Geology* 120: 223–53.

Rochette, P., Folco, L., Suavet, C., van Ginneken, M., Gattacceca, J., Perchiazzi, N., Braucher, R. and Harvey, R. P. 2008. Micrometeorites from the Transantarctic Mountains. *Proceedings of the National Academy of Sciences of the United States of America* 105: 18206–11.

Rubin, A. E. and Grossman, J. N. 2010. Meteorite and meteoroid: New comprehensive definitions. *Meteoritics & Planetary Science* 45(1): 114–22.

Rudraswami, N. G., Prasad, M. S., Plane, J. M. C., Berg, T., Feng, W. and Balgar, S. 2014. Refractory metal nuggets in different types of cosmic spherules. *Geochimica et Cosmochimica Acta* 131: 247–66.

Sanloup, C., Blichert-Toft, J., Télouk, P., Gillet, P. and Albarède, F. 2000. Zr isotope anomalies in chondrites and the presence of 92 Nb in the early solar system. *Earth and Planetary Science Letters* 184: 75–81.

Shiraishi, K., Dunkley, D. J., Hokada, T., Fanning, C. M., Kagami, H. and Hamamoto, T. 2008. Geochronological constraints on the Late Proterozoic to Cambrian crustal evolution of eastern

Dronning Maud Land, East Antarctica: a synthesis of SHRIMP U-Pb age and Nd model age data. *Geological Society*, London, Special Publications 308: 21–67.

Soens, B., Chernonozhkin, S. M., de Vega, C. G., Vanhaecke, F., van Ginneken, M., Claeys, P. and Goderis, S. 2022. Characterization of achondritic cosmic spherules from the Widerøefjellet micrometeorite collection (Sør Rondane Mountains, East Antarctica). *Geochimica et Cosmochimica Acta* 325: 106–28.

Suavet, C., Alexandre, A., Franchi, I., Gattacceca, J., Sonzogni, C., Greenwood, R., Folco, L. and Rochette, P. 2010. Identification of the parent bodies of micrometeorites with high-precision oxygen isotope ratios. *Earth and Planetary Science Letters* 293(3-4): 313–20.

Suttle, M. D. and Folco, L. 2020. The extraterrestrial dust flux: Size distribution and mass contribution estimates inferred from the Transantarctic Mountains (TAM) micrometeorite collection. *Journal of Geophysical Research: Planets* 125(2), e2019JE006241.

Szydlik, P. P. and Flynn, G. J. 1992. The internal temperature profiles of large micrometeorites during atmospheric entry. *Meteoritics* 27(3): 294–5.

Taylor, S., Lever, J. H. and Harvey, R. P. 1998. Accretion rate of cosmic spherules measured at the South Pole. *Nature* 392(6679): 899–903.

Taylor, S., Lever, J. H. and Harvey, R. P. 2000. Numbers, types, and compositions of an unbiased collection of cosmic spherules. *Meteoritics & Planetary Science* 55: 651–66.

Taylor, S., Alexander, C. M. O'D., Delaney, J., Ma, P., Herzog, G. F. and Engrand, C. 2005. Isotopic fractionation of iron, potassium, and oxygen in stony cosmic spherules: Implications for heating histories and sources. *Geochimica et Cosmochimica Acta* 69(10): 2647–62.

Thiemens, M., Jackson, T., Zipf, E., Erdman, P.W. and Van Egmond, C. 1995. Carbon dioxide and oxygen isotope anomalies in the mesosphere and stratosphere. *Science* 270: 969–72.

Trail, D., Watson E. B. and Tailby, N. D. 2012. Ce and Eu anomalies in zircon as proxies for the oxidation state of magmas. *Geochimica et Cosmochimica Acta* 97: 70–87.

van Ginneken, M., Genge, M. J., Folco, L. and Harvey, R. P. 2016. The weathering of micrometeorites from the Transantarctic Mountains. *Geochimica et Cosmochimica Acta* 179: 1–31.

van Ginneken, M., Gattacceca, J., Rochette, P., Sonzogni, C., Alexandre, A., Vidal, V. and Genge, M. J. 2017. The parent body controls on cosmic spherule texture: Evidence from the oxygen isotopic compositions of large micrometeorites. *Geochimica et Cosmochimica Acta* 212: 196–210.

Van Maldeghem, F., Van Ginneken, M., Soens, B., Kaufmann, F., Lampe, S., Krämer Ruggiu, L., Hecht, L., Claeys, P. and Goderis, S. 2023. Geochemical characterization of scoriaceous and unmelted micrometeorites from the Sør Rondane Mountains, East Antarctica: links to chondritic parent bodies and the effects of alteration. *Geochimica et Cosmochimica Acta* 354: 88–108.

Wang J., Davis A. M., Clayton R. N., Mayeda T. K. and Hashimoto A. 2001. Chemical and isotopic fractionation during the evaporation of the FeO-MgO-SiO2-CaO-Al2O3-TiO2-REE melt system. *Geochimica et Cosmochimica Acta* 65: 479–94.

Ward, D., Bischoff, A., Roszjar, J., Berndt, J. and Whitehouse, M. J. 2017. Trace element inventory of meteoritic Ca-phosphates. *American Mineralogist: Journal of Earth and Planetary Materials* 102(9): 1856–80.

Yada, T., Stadermann, F. J., Floss, C., Zinner, E., Olinger, C. T., Graham, G. A., Bradley, J. P., Dai, Z. R., Nakamura, T., Noguchi, T. and Bernas, M. 2005. Discovery of abundant presolar silicates in subgroups of Antarctic micrometeorites. *36th Annual Lunar and Planetary Science Conference*, League City, Texas, March 14–18, 2005, abstract no. 1227.

8. Tables & Figures

Table 1. Overview of the selected samples. The listed textural types (V, CC, BO, Po) refer to a vitreous, cryptocrystalline, barred olivine, and porphyric texture, respectively. The classification of Cordier is also applied to the particles studied and listed in the table. Furthermore, the level of weathering, using the scale developed by van Ginneken et al. (2016), is also listed below. In addition, an overview is provided of the degrees of evaporation (DoE) for the samples studied, based on multiple proxies (Sc+Y+Zr+Hf, Al+Ca+Ti, Mg/Al). Evaporation proxies based on $\delta^{18}O$ are also provided, where the Rayleigh fractionation law is applied, and the listed values are calculated as DoE = $(R/R_0)^{-1/(\alpha - 1)}$. Finally, the average REE_N values (normalized to CI chondrites; Lodders, 2003) are also provided.

Sample	Size[1] (µm)	Textural type	Classification (Cordier et al., 2011)	Weathering level (van Ginneken et al., 2016)	DoE (ScYZrHf based)	DoE (AlCaTi based)	DoE (Mg/Al based)	DoE ($^{18}O/^{16}O$ based)	Average REE_N
WF18-0502	129.9	V	'CAT-like'	0a	0.96	0.80	0.99	0.83	47.96
WF18-0504	163.0	V	'CAT-like'	0a	0.97	0.81	0.99	0.86	54.10
WF18-0506	188.8	V	'CAT-like'	1a	0.74	0.69	0.66	0.67	6.81
WF18-0221	236.7	CC/BO	'CAT-like'	0a	0.79	0.78	0.99	0.79	10.90
WF18-0224	215.9	CC/BO	'CAT-like'	0a	0.91	0.89	0.90	n.a.	11.53
WF18-0229	209.7	BO	'CAT-like'	1a	0.90	0.78	0.04	n.a.	6.32
WF18-0231	193.8	BO	'CAT-like'	1a	0.84	0.82	0.70	n.a.	6.52
WF18-0208	265.4	BO	'CAT-like'	1b	0.52	0.56	0.10	0.19	2.30
WF18-0413	190.2	CC/BO	'CAT-like'	0a	0.95	0.90	0.98	0.31	20.88
WF18-0416	184.3	CC/BO	'CAT-like'	0b	0.91	0.76	1.00	n.a.	10.51
WF18-0425	198.5	Scoriaceous	'CAT-like'	1b	0.87	0.85	0.99	n.a.	16.99
WF18-0415	141.5	CC	'CAT-like'	n.a.	0.82	0.83	0.85	n.a.	9.31
WF18-0227	260.5	V	'CAT-like'	2c	0.94	0.94	0.94	0.11	17.30
WF18-0207	208.3	CC/BO	'CAT-like'	0b	0.91	0.79	1.00	0.87	16.65
WF18-0419	155.0	CC/BO	'CAT-like'	1a	0.83	0.84	0.97	0.69	8.02
WF18-AD1	n.a.	BO	'CAT-like'	n.a.	0.70	0.71	0.65	n.a.	4.17
WF18-AD2	n.a.	BO	'CAT-like'	n.a.	0.93	0.90	0.98	n.a.	12.05
WF18-AD3	n.a.	BO	'CAT-like'	n.a.	0.84	0.74	0.98	n.a.	8.92
WF18-AD4	n.a.	BO	'CAT-like'	n.a.	0.77	0.74	0.55	n.a.	3.66
WF18-AD5	n.a.	BO	'CAT-like'	n.a.	0.84	0.82	0.73	n.a.	5.11
WF18-AD6	n.a.	BO	'CAT-like'	n.a.	0.84	0.81	0.79	n.a.	4.68
WF18-AD7	n.a.	BO	'CAT-like'	n.a.	0.82	0.75	0.83	n.a.	4.66
WF18-AD8	n.a.	BO	'CAT-like'	n.a.	0.89	0.82	0.79	n.a.	5.01
WF18-AD9	n.a.	BO	'CAT-like'	n.a.	0.74	0.72	0.58	n.a.	3.28
WF18-AD10	n.a.	BO	'CAT-like'	n.a.	0.91	0.87	0.90	n.a.	9.92
WF18-0501	141.5	V	'normal chondritic'	1a	0.59	0.54	0.37	0.67	2.76
WF18-0505	192.1	V	'normal chondritic'	0a	0.66	0.61	0.59	0.59	5.61
WF18-0507	171.7	V	'normal chondritic'	0a	0.58	0.35	0.43	0.15	2.15
WF18-0508	183.5	V	'normal chondritic'	0a	0.37	-0.61	-0.61	0.40	0.84
WF18-0509	160.4	V	'normal chondritic'	0a	0.54	0.59	0.40	0.73	1.92

WF18-0512	143.2	V	'normal chondritic'	1a	0.59	0.48	0.41	0.25	2.62
WF18-0513	177.7	V	'normal chondritic'	1a	0.69	0.60	0.71	0.48	12.39
WF18-0514	159.6	V	'normal chondritic'	1a	0.72	0.65	0.58	0.58	4.27
WF18-0209	247.4	Po	'normal chondritic'	1b	0.84	0.46	0.38	0.24	5.35
WF18-0204	204.1	BO	'normal chondritic'	2c	0.69	0.25	-0.40	0.23	2.27
WF18-0201	194.7	n.a.	n.a.	n.a.	n.a.	n.a.	n.a.	0.44	n.a.
WF18-0214	293.7	n.a.	n.a.	n.a.	n.a.	n.a.	n.a.	1.66	n.a.
WF18-0215	274.4	n.a.	n.a.	n.a.	n.a.	n.a.	n.a.	0.40	n.a.
WF18-0403	131.8	n.a.	n.a.	n.a.	n.a.	n.a.	n.a.	0.25	n.a.

[1] It should be noted that these values are estimates; cosmic spherules have three-dimensional curvature, while BSE images are two-dimensional. Using these images, two perpendicular diameters were measured using the SEM-EDS software. The particle size listed was calculated as the cube root of the product of the longest measured diameter and the square of the shortest measured diameter. Thus, the listed particle sizes are calculated sizes from apparent diameters, not absolute sizes.

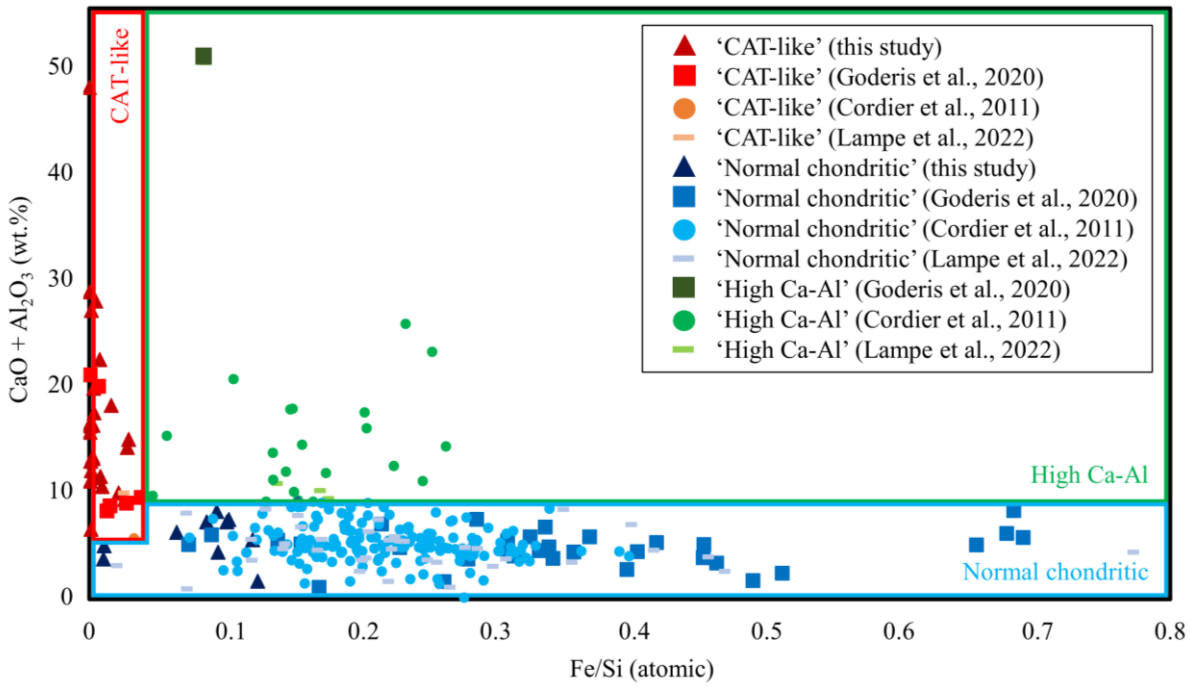

***Fig. 1**. Fe/Si vs CaO + Al_2O_3 plot comparing data from this study with data for 'normal chondritic', 'CAT-like' and 'High Ca-Al' data of Cordier et al. (2011), Goderis et al. (2020) and Lampe et al. (2022).*

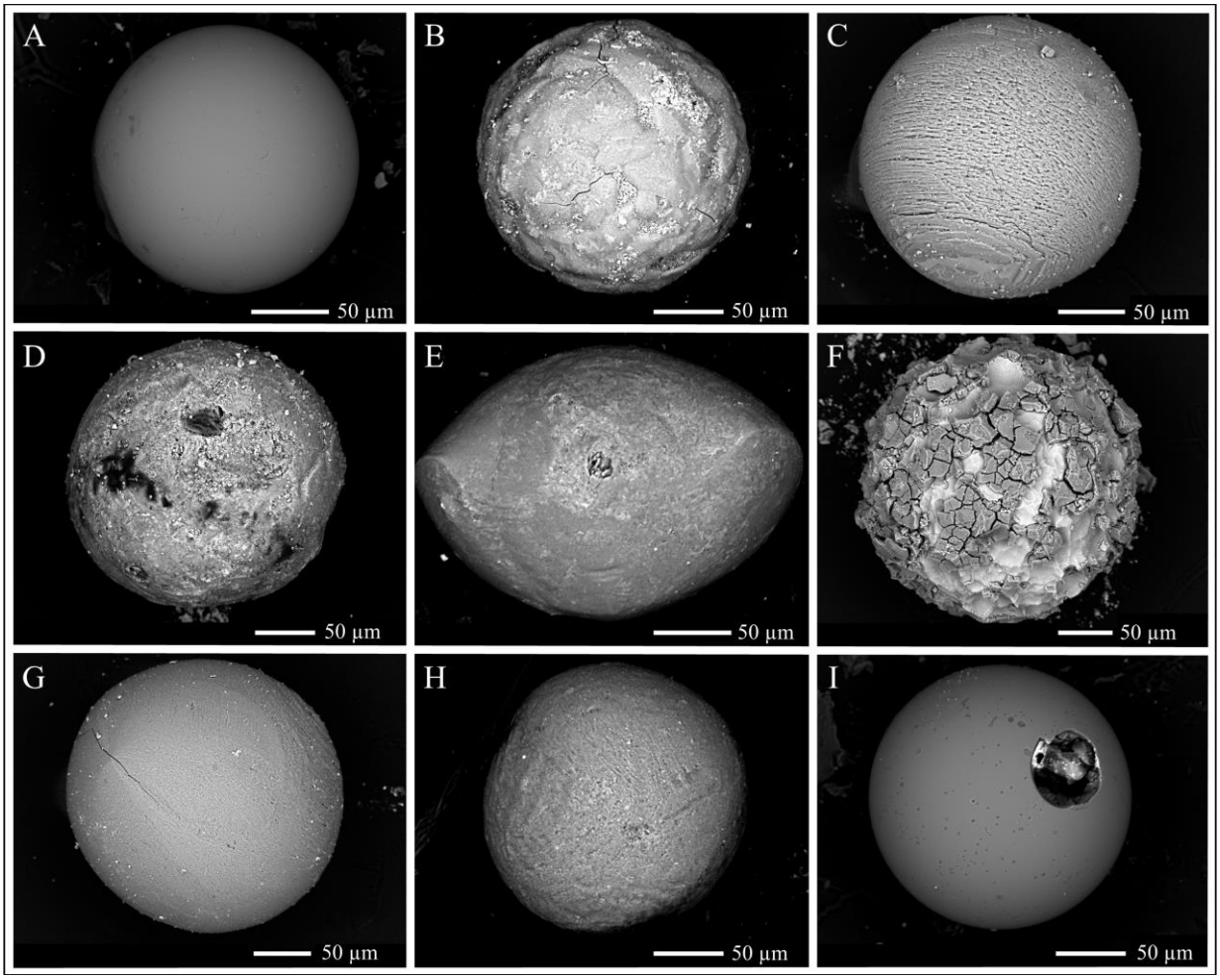

***Fig. 2**. Selected BSE images of samples studied, acquired with SEM-EDS. (a) Sample WF18-0507 (V-type). (b) Sample WF18-0201 (CC-type). (c) Sample WF18-0229 (BO-type). (d) Sample WF18-0204 (Po-type). (e) Sample WF18-0425 (Scoriaceous). (f) Sample WF18-0227 (severely altered V-type or terrestrial particle). (g) Sample WF18-0221 (CC/BO-type hybrid). (h) Sample WF18-0413 (can be classified as both CC-type and BO-type). (i) Sample WF18-0506 (V-type cosmic spherule with a significant cavity present, presumably remnant of an ejected metal bead).*

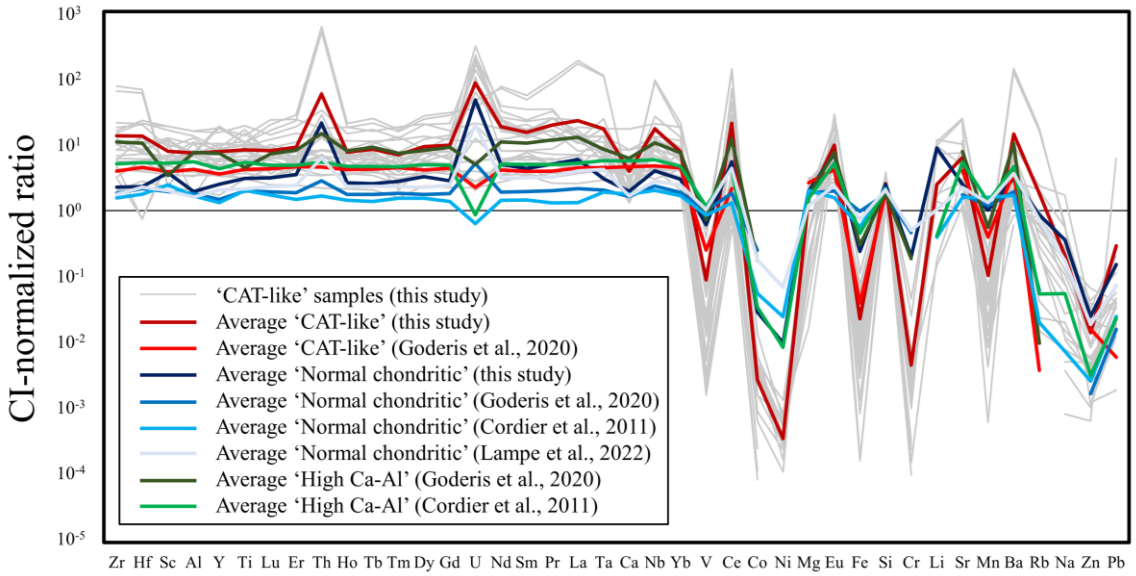

***Fig. 3**. Elemental patterns of all 'CAT-like' samples of this study analysed by LA-ICP-MS, compared with averages found in literature (Cordier et al., 2011; Goderis et al., 2020; Lampe et al., 2021). The elements on the horizontal axis are arranged according to their respective 50 % condensation temperatures at 10^{-4} atm, and are thus a measure of their volatility (Lodders, 2003). The logarithmic vertical axis gives an indication of the relative degree of enrichment of an element as compared to normal CI chondrite values. Discontinuities in curves indicate that the calculated concentration (in µg/g) was below the limit of detection, and these concentrations are therefore not included on the plot.*

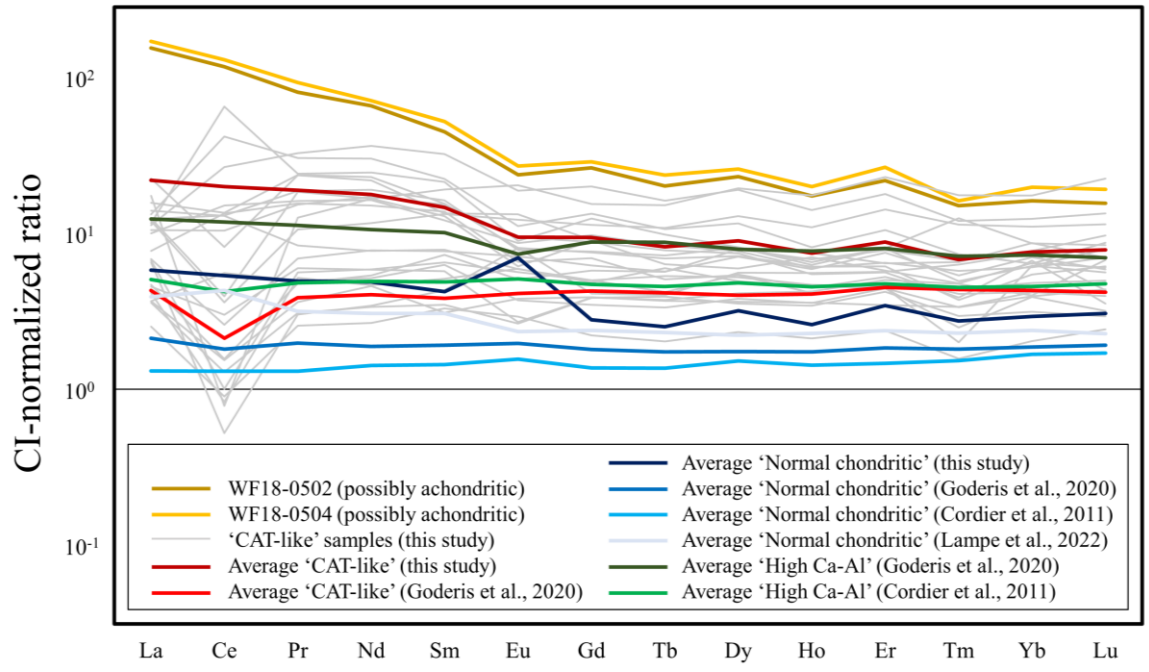

***Fig. 4**. REE patterns[2] for the samples analysed, compared with averages found in literature (Cordier et al., 2011; Goderis et al., 2020; Lampe et al., 2021). The elements on the horizontal axis are arranged according to increasing volatility order. The logarithmic vertical axis gives an indication of the relative degree of enrichment of an element as compared to normal CI chondrite values.*

[2] The rare earth elements (REEs) comprise of the entire lanthanide series, with the addition of Sc and Y. Thus, an alternative, more appropriate term for 'REE patterns' could be 'lanthanide patterns'. Nevertheless, the term 'REE patterns' is widely used through literature (Cordier et al., 2011; Cordier et al., 2012; Goderis et al., 2020; Greshake, 1996; Presper et al., 1993; Szydlik & Flynn, 1992), and is for the sake of consistency with literature also used throughout the remainder of this study.

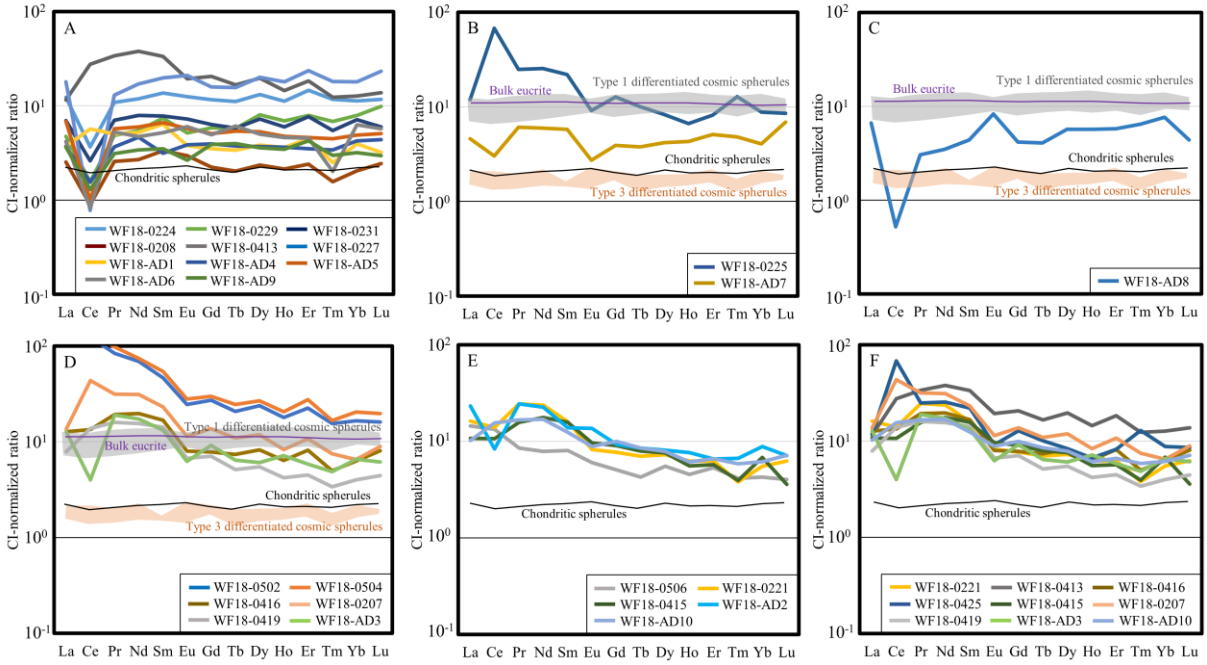

***Fig. 5**. The categories of REE patterns observed in this study (normalization to CI chondritic values from McDonough & Sun (1995)). Patterns of bulk eucrites (Kitts and Lodders, 1998; Barrat et al., 2007) and chondritic spherules from the Transantarctic Mountains (TAM) collection were added, along with shaded envelopes of Types 1 and 3 differentiated cosmic spherules (cfr. Cordier et al., 2012). (A) Flat, non-fractionated, chondrite-like REE patterns ($(La/Yb)_N = 0.6 – 1.5$ and $Eu^* = 0.7 – 1.3$) (N = 11). (B) Flat, non-fractionated, chondrite-like REE patterns with negative Eu anomalies ($(La/Yb)_N = 0.6 – 1.5$ and $Eu^* < 0.7$) (N = 2). (C) Flat, non-fractionated, chondrite-like REE pattern with a positive Eu anomaly ($(La/Yb)_N = 0.6 – 1.5$ and $Eu^* > 1.3$) (N= 1). (D) LREE-enriched REE patterns with a negative Eu anomaly ($(La/Yb)_N > 1.5$ and $Eu^* < 0.7$) (N = 6). (E) LREE-enriched REE patterns ($(La/Yb)_N > 1.5$ and $Eu^* = 0.7 – 1.3$) (N = 5); these patterns show variations from the types previously identified by Goderis et al (2020), particularly in La and LREE enrichments, underscoring the importance of a visual inspection of the REE patterns alongside with La/Yb ratios. (F) REE patterns with enhanced Pr, Nd and Sm enrichments, resulting in bulged profiles (N = 9).*

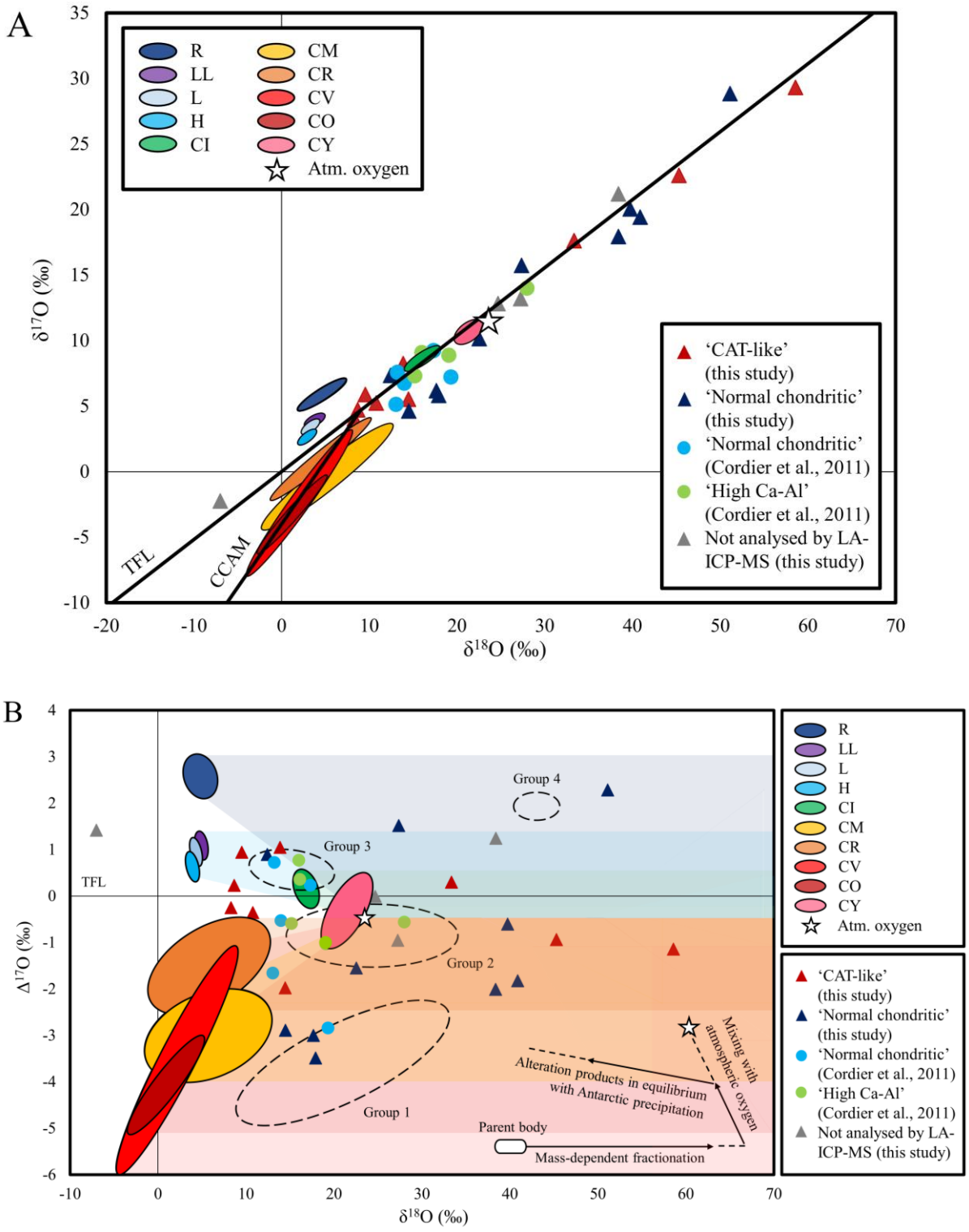

***Fig. 6**. (A) $\delta^{18}O$ vs $\delta^{17}O$ plot comparing data from this study with Cordier et al. (2011). (B) $\delta^{18}O$ vs $\Delta^{17}O$ plot comparing data from this study with Cordier et al.(2011). The dotted outlines of 4 groups represent the various groups that have been classified by Suavet et al. (2010). Delta values are expressed in ‰ relative to V-SMOW. In both plots, colored domains represent potential parent bodies (Clayton et al., 1991; Clayton & Mayeda, 1999). The chondrite fields CO, CV, CM, CR, CY and CI highlight carbonaceous chondrites (CC), the chondrite fields H, L and LL represent ordinary chondrites (OC), and R represents the rare Rumuruti-type meteorites (Suavet et al., 2010). A star represents the average isotopic composition of atmospheric oxygen at the transition between the stratosphere and mesosphere ($\delta^{18}O \approx 23.5$ ‰ and $\delta^{18}O \approx 11.8$ ‰; $\Delta^{17}O \approx -0.42$ ‰) (Thiemens et al., 1995). TFL = Terrestrial Fractionation Line. CCAM = Carbonaceous Chondrite Anhydrous Minerals line. Both plots were adapted from Suavet et al. (2010).*

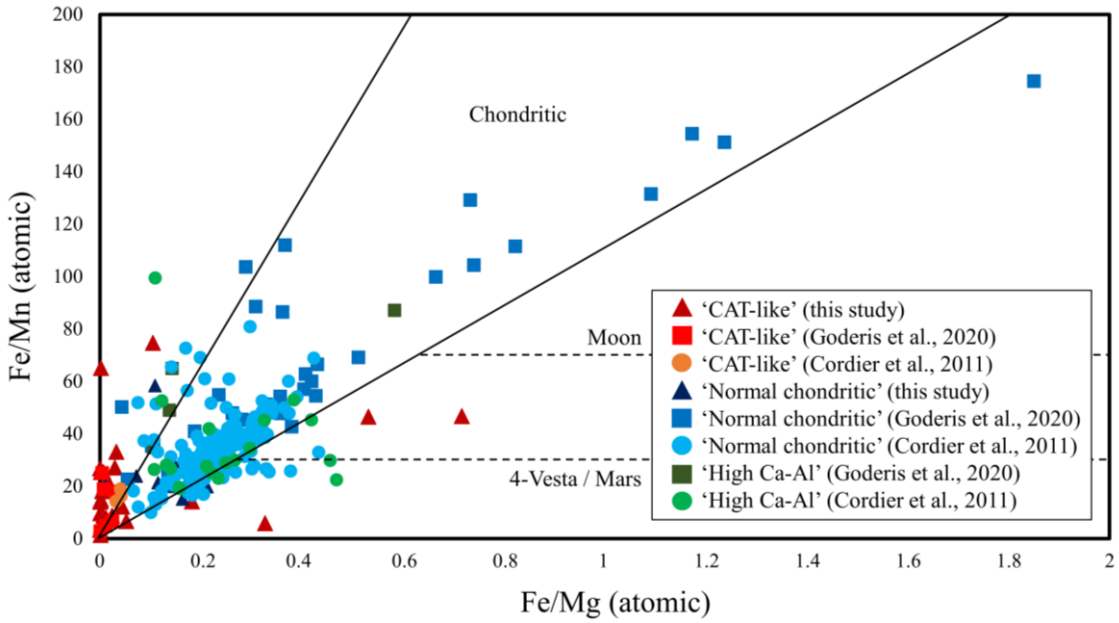

***Fig. 7**. Fe/Mg vs Fe/Mn plot comparing data from this study with data of 'normal chondritic', 'CAT-like' and 'High Ca-Al' data of Cordier et al. (2011) and Goderis et al. (2020).*

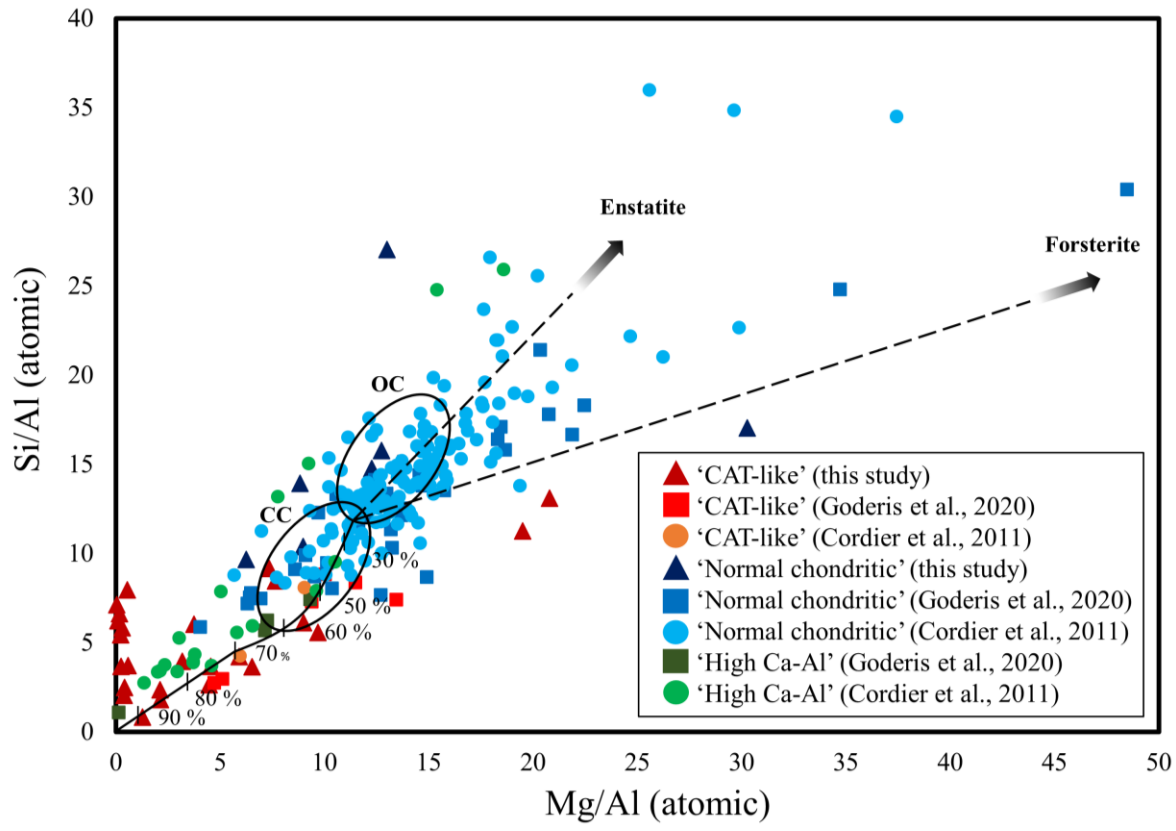

***Fig. 8**. Mg/Al vs Si/Al plot comparing data from this study with data of 'normal chondritic', 'CAT-like' and 'High Ca-Al' data of Cordier et al. (2011) and Goderis et al. (2020). OC: Ordinary Chondritie field; CC: Carbonaceous Chondrite field. The evaporation line and respective evaporation percentages are modelled according to Taylor et al. (2005). The line originating from the chondritic fields towards the origin of the diagram reflects increased evaporation. The arrows labelled as 'Enstatite' and 'Forsterite' illustrate the mineralogical control on the respective spherule.*

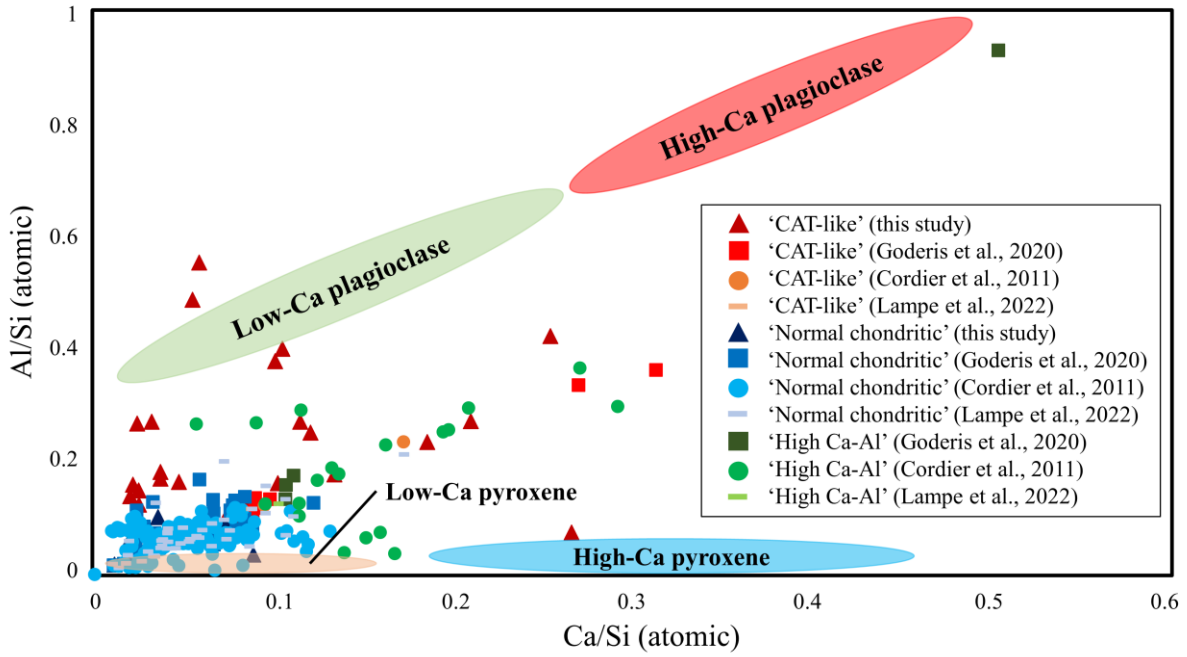

***Fig. 9**. Distribution of 'Normal chondritic', 'CAT-like' and 'High Ca-Al' cosmic spherules in Al/Si vs Ca/Si space (Soens et al., 2022). It must be noted that the plagioclase fields represent a chemical composition range, but the physical form of these materials might have been amorphized to maskelynite following shock metamorphosis. Reference values for low-Ca plagioclase (often amorphized to maskelynite) were reproduced from Papike et al. (2009). Pyroxene and high-Ca plagioclase values were adapted from Mittlefehldt (1994).*

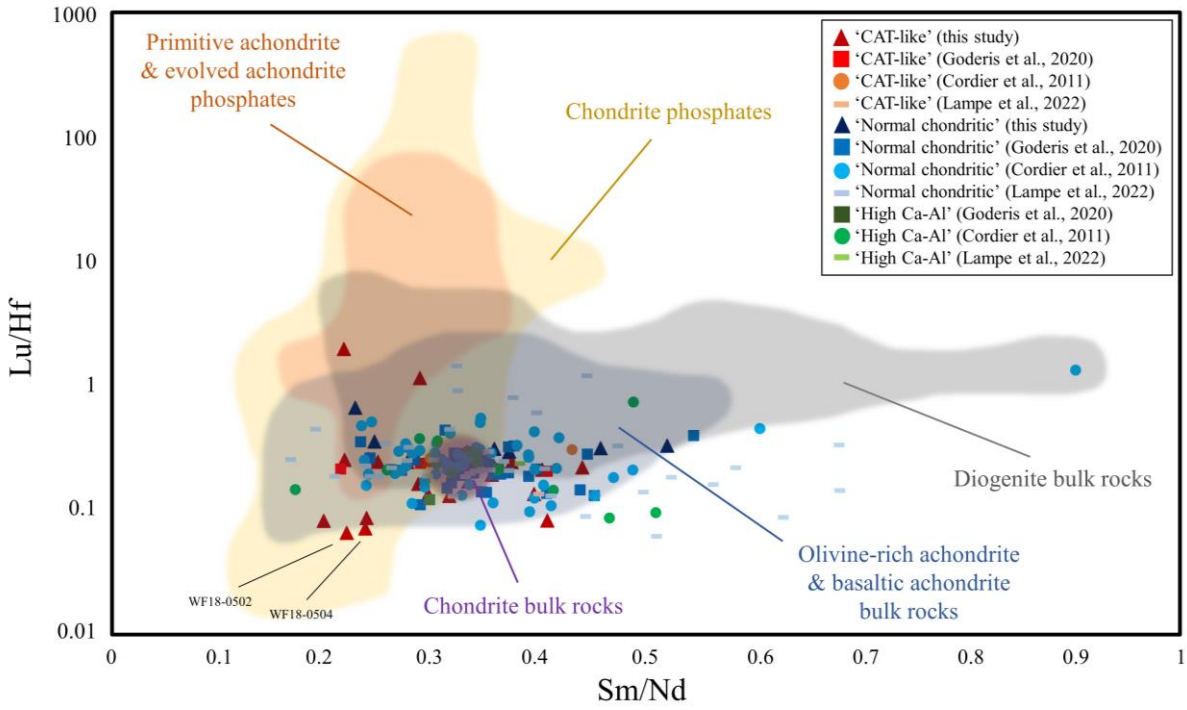

***Fig. 10**. Comparative diagram of Sm/Nd vs Lu/Hf ratios for the cosmic spherules studied, selected literature data, meteoritic phosphate data (chondrites, primitive achondrites & evolved achondrites), and meteoritic bulk rock data (chondrites, diogenites, olivine-rich achondrites & basaltic achondrites). The shaded areas that cover phosphate and bulk rock data are adapted from Chernonozhkin et al. (2021) and references therein.*

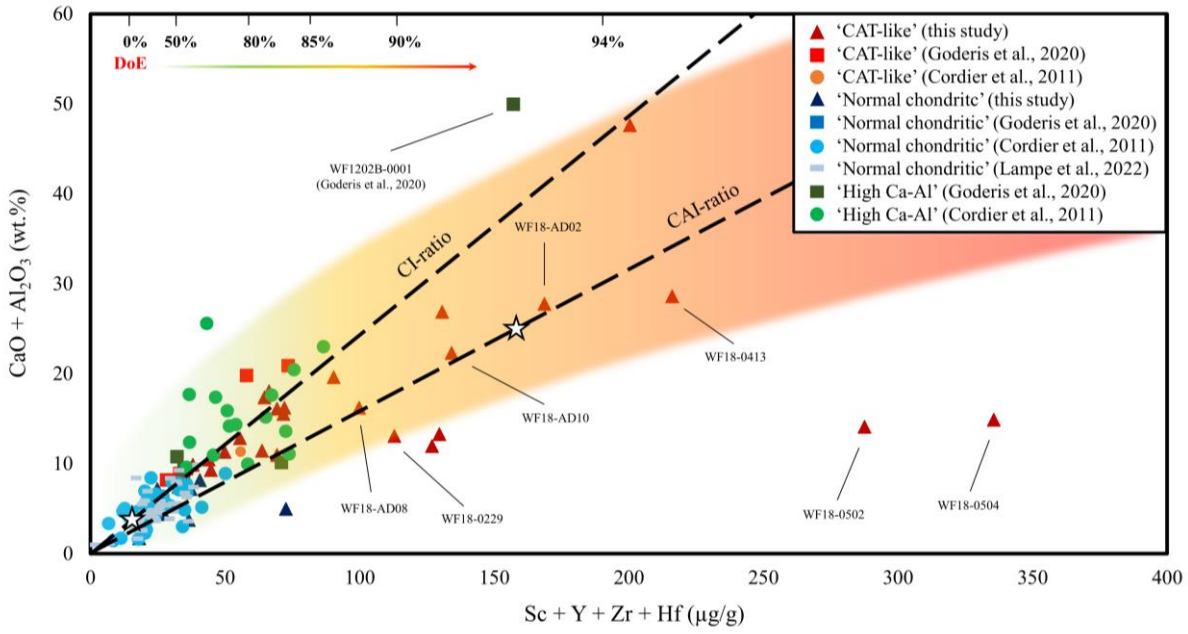

Fig. 11. *Sc + Y + Zr + Hf vs CaO + Al_2O_3 plot comparing data from this study with literature data (Cordier et al., 2011; Goderis et al., 2020; Lampe et al., 2021). The dashed diagonal CI-ratio line depicts the ratio of Sc + Y + Zr + Hf (µg/g) to CaO + Al_2O_3 (wt.%) for CI chondrites, modelled according to data of McDonough & Sun (1995). The data point corresponding to recommended CI-chondritic concentrations is marked with a star (Sc + Y + Zr + Hf (µg/g) = 11.4; CaO + Al_2O_3 (wt.%) = 2.9). In an analogical way, the dashed diagonal CAI-ratio line depicts the ratio of Sc + Y + Zr + Hf (µg/g) to CaO + Al_2O_3 (wt.%) for CAI inclusions, modelled according to averaged data of Kimura et al. (1993). The shaded area illustrates the region in which most data points plot. With increasing refractory element content, and thus a higher degree of evaporation (DoE), a clear deviation from the CI-ratio becomes observable, and more data points plot closer to the CAI-ratio. The six data points that are deemed to be dominated by a single Al- and Ca-rich phase (WF18-0229, 0413, AD02, AD08, AD10 and WF1202B-0001; Goderis et al., 2020) are highlighted, along with the two potentially achondritic particles (WF18-0502 and 0504).*

Appendix

Table A.1. Mass fractions of major element oxides in 10 'normal chondritic' cosmic spherules as determined with LA-ICP-MS.

	WF18-0501	WF18-0505	WF18-0507	WF18-0508	WF18-0509	WF18-0512	WF18-0513	WF18-0514	WF18-0209	WF18-0204
SiO_2 (wt.%)	55.6	59.1	56.9	60.8	62.8	55.7	59.1	54.0	55.0	43.6
TiO_2	0.22	0.21	0.17	0.15	0.14	0.17	0.19	0.25	0.50	0.22
Al_2O_3	3.13	3.60	3.27	1.01	1.97	2.99	5.19	4.41	3.64	2.17
FeO	4.30	7.31	6.48	9.07	7.64	8.04	6.15	6.09	0.72	0.54
MnO	0.18	0.48	0.30	0.43	0.38	0.29	0.30	0.10	0.04	0.03
MgO	33.5	25.1	31.7	27.8	20.2	30.1	25.6	31.3	38.6	51.9
CaO	3.11	3.84	1.13	0.69	5.23	2.55	2.01	3.78	1.36	1.58
Na_2O	<LOD	0.19	<LOD	0.00	1.15	<LOD	1.06	0.01	0.07	0.00
CaO + Al_2O_3 (wt.%)	6.24	7.43	4.40	1.70	7.20	5.54	7.20	8.19	5.00	3.75
Fe/Mn (atomic)	23.9	15.1	21.4	21.0	19.9	27.6	20.0	58.4	20.3	19.6
Fe/Mg	0.07	0.16	0.11	0.18	0.21	0.15	0.13	0.11	0.01	0.01
Fe/Si	0.06	0.10	0.10	0.12	0.10	0.12	0.09	0.09	0.01	0.01
Mg/Si	0.90	0.63	0.83	0.68	0.48	0.81	0.65	0.86	1.05	1.78
Ca/Si	0.06	0.07	0.02	0.01	0.09	0.05	0.04	0.07	0.03	0.04
Si/Al	15.0	13.9	14.8	51.0	27.1	15.8	9.67	10.4	12.8	17.0
Mg/Al	13.5	8.82	12.3	34.7	13.0	12.7	6.25	8.97	13.4	30.3

Table A.2. Mass fractions of trace elements in 10 'normal chondritic' cosmic spherules, as determined with LA-ICP-MS.

	WF18-0501	WF18-0505	WF18-0507	WF18-0508	WF18-0509	WF18-0512	WF18-0513	WF18-0514	WF18-0209	WF18-0204
Li (µg/g)	<LOD	127	<LOD	<LOD	0.23	0.21	2.74	0.34	<LOD	<LOD
Sc	15.4	19.6	14.5	12.3	14.5	15.8	17.3	22.0	62.8	23.5
V	59.7	18.7	16.8	23.6	84.5	61.4	44.9	28.4	2.02	1.84
Cr	343	1130	23.4	20.8	2660	1129	32.8	16.4	7.52	0.44
Co	5.02	64.5	3.89	1.15	13.2	42.5	9.86	6.80	0.74	0.10
Ni	0.33	257	0.38	<LOD	215	583	5.59	0.17	1.57	<LOD
Zn	0.23	23.4	<LOD	1.17	21.8	0.19	19.4	0.26	11.5	0.69
Rb	0.07	0.08	0.02	1.30	6.17	<LOD	11.08	0.11	1.03	<LOD
Sr	18.2	26.6	7.51	5.54	8.15	11.7	67.2	28.9	3.05	3.07
Y	3.63	4.12	3.24	0.80	2.59	3.51	7.09	5.43	4.97	3.71
Zr	8.31	8.69	9.38	4.83	7.50	8.47	12.36	12.75	4.61	9.06
Nb	0.86	2.25	0.76	0.47	0.66	0.73	1.64	1.13	0.24	0.77
Ba	4.03	5.05	3.43	1.70	2.74	4.73	43.06	8.47	0.96	1.15
La	0.66	0.68	0.37	0.35	0.41	0.58	8.32	1.12	1.14	0.37
Ce	1.54	2.43	0.95	0.58	0.98	1.37	18.42	2.94	3.34	0.80
Pr	0.22	0.27	0.13	0.06	0.15	0.24	1.96	0.40	1.07	0.16
Nd	1.40	1.47	0.87	0.41	0.73	1.14	8.12	2.19	5.36	0.94
Sm	0.45	0.49	0.32	0.21	0.26	0.36	1.99	0.61	1.22	0.43
Eu	0.18	2.46	0.10	0.01	0.12	0.16	0.50	0.26	0.16	0.04
Gd	0.50	0.38	0.48	0.06	0.34	0.54	1.46	0.72	0.74	0.38
Tb	0.09	0.08	0.07	0.01	0.08	0.07	0.19	0.13	0.12	0.08
Dy	0.69	0.57	0.61	0.16	0.51	0.78	1.78	1.09	1.06	0.69
Ho	0.15	0.10	0.13	0.03	0.10	0.13	0.30	0.20	0.16	0.13
Er	0.52	0.36	0.52	0.11	0.41	0.57	1.09	0.79	0.66	0.55
Tm	0.06	0.08	0.06	0.02	0.05	0.06	0.11	0.09	0.09	0.06
Yb	0.48	0.45	0.33	0.20	0.34	0.43	0.82	0.62	0.61	0.48
Lu	0.06	0.05	0.06	0.04	0.05	0.07	0.13	0.11	0.11	0.08
Hf	0.22	0.17	0.21	0.12	0.15	0.26	0.36	0.44	0.17	0.26
Ta	0.04	0.06	0.04	0.03	0.04	0.04	0.06	0.05	0.01	0.04
Pb	0.01	1.07	0.01	0.12	0.00	0.00	2.46	0.04	0.08	0.01
Th	0.07	2.58	0.07	0.10	0.07	0.06	2.58	0.17	0.26	0.08
U	0.01	0.89	<LOD	0.02	0.02	0.01	0.79	0.02	1.62	0.06
Sc + Y + Zr + Hf (µg/g)	27.5	32.6	27.3	18.1	24.8	28.0	37.2	40.6	72.5	36.6
$(La/Yb)_N$	0.92	1.03	0.75	1.21	0.82	0.92	6.88	1.23	1.28	0.52
$(La/Pr)_N$	1.18	0.98	1.09	2.18	1.09	0.95	1.66	1.09	0.42	0.90
Ce*	0.86	1.30	0.90	0.82	0.96	0.90	1.20	1.00	0.73	0.73
Eu*	1.17	17.4	0.78	0.35	1.24	1.13	0.90	1.19	0.51	0.34
Tm*	0.83	1.22	0.96	0.88	0.95	0.79	0.78	0.81	0.89	0.77
Avg. REE_N	2.76	5.61	2.15	0.84	1.92	2.62	12.4	4.27	5.35	2.27

Table A.3. Mass fractions of major element oxides in 25 'CAT-like' cosmic spherules as determined with LA-ICP-MS (part 1).

	WF18-0502	WF18-0504	WF18-0506	WF18-0221	WF18-0224	WF18-0229	WF18-0231	WF18-0208	WF18-0413	WF18-0416	WF18-0425	WF18-0415	WF18-0227	WF18-0207	WF18-0419
SiO_2 (wt.%)	78.2	78.1	57.2	84.7	45.1	41.8	37.9	43.1	61.4	86.5	75.2	53.0	25.3	84.6	71.8
TiO_2	0.77	0.78	0.28	0.56	0.69	0.41	0.43	0.22	1.39	0.69	0.74	0.63	0.99	0.80	0.67
Al_2O_3	11.4	12.1	5.30	10.8	16.2	2.71	8.78	3.25	25.4	10.3	17.3	11.4	25.7	11.5	16.4
FeO	2.63	2.72	1.79	0.12	0.09	0.14	0.13	0.07	0.02	0.16	0.30	0.22	0.00	0.26	1.40
MnO	0.06	0.06	0.05	0.01	0.01	0.00	0.01	0.00	0.01	0.03	0.04	0.01	0.00	0.02	0.02
MgO	2.78	2.13	30.8	1.49	27.2	44.5	45.3	50.1	8.09	0.28	3.27	28.6	26.0	0.82	7.53
CaO	2.75	2.75	4.00	2.03	10.7	10.4	7.43	3.27	3.19	1.69	2.31	6.00	22.0	1.77	1.67
Na_2O	0.43	0.39	1.17	0.13	0.04	0.00	0.01	<LOD	0.16	0.12	0.38	0.06	0.00	0.09	0.19
$CaO + Al_2O_3$ (wt.%)	14.13	14.88	9.30	12.85	26.90	13.10	16.22	6.51	28.61	11.98	19.65	17.37	47.64	13.29	18.05
Fe/Mn (atomic)	46.6	46.7	33.2	12.3	15.0	65.2	25.4	14.3	1.47	5.98	6.73	18.1	26.8	14.2	74.7
Fe/Mg	0.53	0.72	0.03	0.04	0.00	0.00	0.00	0.00	0.00	0.33	0.05	0.00	0.00	0.18	0.10
Fe/Si	0.03	0.03	0.03	0.00	0.00	0.00	0.00	0.00	0.00	0.00	0.00	0.00	0.00	0.00	0.02
Mg/Si	0.05	0.04	0.80	0.03	0.90	1.59	1.78	1.73	0.20	0.00	0.06	0.80	1.53	0.01	0.16
Ca/Si	0.04	0.04	0.08	0.03	0.25	0.27	0.21	0.08	0.06	0.02	0.03	0.12	0.93	0.02	0.02
Si/Al	5.83	5.46	9.16	6.64	2.36	13.1	3.66	11.3	2.05	7.14	3.68	3.95	0.84	6.23	3.72
Mg/Al	0.31	0.22	7.35	0.17	2.12	20.8	6.53	19.5	0.40	0.03	0.24	3.18	1.28	0.09	0.58

Table A.4. Mass fractions of major element oxides in 25 'CAT-like' cosmic spherules as determined with LA-ICP-MS (part 2).

	WF18-AD1	WF18-AD2	WF18-AD3	WF18-AD4	WF18-AD5	WF18-AD6	WF18-AD7	WF18-AD8	WF18-AD9	WF18-AD10
SiO_2 (wt.%)	54.9	63.3	84.2	40.8	43.1	45.9	61.7	39.0	44.7	42.5
TiO_2	0.27	1.21	0.49	0.22	0.36	0.40	0.38	0.40	0.23	1.07
Al_2O_3	5.50	21.5	8.97	6.20	8.64	10.6	8.67	12.5	6.19	20.0
FeO	1.43	0.37	0.08	0.14	0.03	0.03	0.62	0.00	0.51	0.40
MnO	0.16	0.01	0.01	0.03	0.00	0.00	0.03	0.00	0.06	0.02
MgO	33.3	7.07	3.81	47.5	40.3	38.1	25.6	44.4	44.0	33.5
CaO	4.39	6.23	2.03	5.12	7.49	4.94	2.77	3.69	4.30	2.35
Na_2O	0.02	0.12	0.05	0.00	0.01	0.01	0.12	0.01	0.01	0.07
$CaO + Al_2O_3$ (wt.%)	9.89	27.77	11.00	11.32	16.13	15.54	11.44	16.23	10.49	22.31
Fe/Mn (atomic)	8.75	27.1	7.88	5.01	14.2	9.71	22.5	3.53	8.64	25.4
Fe/Mg	0.02	0.03	0.01	0.00	0.00	0.00	0.01	0.00	0.01	0.01
Fe/Si	0.02	0.00	0.00	0.00	0.00	0.00	0.01	0.00	0.01	0.01
Mg/Si	0.90	0.17	0.07	1.73	1.39	1.24	0.62	1.70	1.47	1.18
Ca/Si	0.09	0.11	0.03	0.13	0.19	0.12	0.05	0.10	0.10	0.06
Si/Al	8.48	2.49	7.97	5.59	4.23	3.68	6.03	2.64	6.13	1.81
Mg/Al	7.65	0.42	0.54	9.68	5.90	4.55	3.74	4.48	8.99	2.12

Table A.5. Mass fractions of trace elements in 25 'CAT-like' cosmic spherules as determined with LA-ICP-MS (part 1).

	WF18-0502	WF18-0504	WF18-0506	WF18-0221	WF18-0224	WF18-0229	WF18-0231	WF18-0208	WF18-0413	WF18-0416	WF18-0425	WF18-0415	WF18-0227	WF18-0207	WF18-0419
Li (µg/g)	14.2	16.3	10.7	<LOD	<LOD	<LOD	<LOD	<LOD	0.27	2.06	<LOD	<LOD	<LOD	<LOD	0.22
Sc	13.7	14.0	20.8	32.6	73.2	64.0	40.6	13.4	110	67.1	38.9	38.2	109.64	69.6	27.1
V	29.7	22.0	33.3	0.97	1.26	1.15	0.71	0.12	0.34	0.74	3.54	0.87	0.19	1.29	6.48
Cr	125	67.6	8.59	6.86	8.35	4.43	3.67	0.28	0.43	15.9	21.9	4.50	3.17	7.34	10.3
Co	2.10	2.26	2.12	0.84	0.47	0.13	0.33	0.04	1.26	3.19	7.01	0.82	0.06	2.40	2.38
Ni	3.48	2.78	4.15	3.15	2.60	<LOD	1.21	<LOD	7.81	9.33	7.46	8.27	<LOD	4.08	6.46
Zn	0.38	<LOD	10.1	3.02	1.28	0.33	1.92	0.40	13.6	4.55	7.58	2.64	0.21	6.56	9.01
Rb	36.9	40.0	5.42	1.42	0.46	<LOD	0.54	<LOD	1.83	1.83	4.70	1.77	<LOD	1.34	2.24
Sr	169	177	53.4	8.82	81.4	7.49	44.3	19.6	21.3	7.06	9.53	39.2	144	9.46	8.47
Y	27.3	29.3	7.45	10.9	16.1	9.27	9.52	2.68	23.7	13.5	12.9	8.46	27.4	15.4	7.21
Zr	240	285	16.1	12.0	40.3	38.5	21.3	7.60	80.3	45.4	37.9	17.9	61.0	43.7	31.3
Nb	21.0	22.0	1.60	2.72	3.14	2.56	0.98	1.01	6.26	3.01	3.81	1.93	4.90	3.96	2.32
Ba	290	334	23.42	3.64	15.3	1.45	8.90	5.17	5.12	2.01	6.75	11.4	18.4	3.66	3.25
La	38.7	42.7	3.41	3.84	2.92	1.12	1.65	0.60	2.75	3.02	2.83	2.55	4.25	3.23	1.87
Ce	75.6	83.9	8.17	8.54	2.24	0.96	1.60	0.55	16.9	8.21	41.7	6.55	0.48	26.7	8.48
Pr	7.81	9.06	0.79	2.27	1.01	0.45	0.65	0.24	3.14	1.79	2.31	1.46	1.20	2.93	1.49
Nd	31.5	33.9	3.60	10.9	5.45	2.50	3.63	1.23	17.3	8.99	11.6	8.07	7.82	14.3	7.09
Sm	6.92	8.04	1.19	2.36	2.02	1.10	1.16	0.49	4.96	2.48	3.26	2.33	2.93	3.42	2.10
Eu	1.38	1.58	0.34	0.46	0.71	0.29	0.41	0.17	1.09	0.45	0.52	0.54	1.19	0.64	0.38
Gd	5.42	5.94	1.01	1.53	2.31	1.17	1.26	0.44	4.10	1.55	2.54	1.80	3.16	2.73	1.41
Tb	0.75	0.88	0.15	0.25	0.40	0.21	0.21	0.07	0.60	0.27	0.36	0.29	0.56	0.39	0.19
Dy	5.88	6.58	1.36	1.79	3.25	1.98	1.78	0.58	4.83	2.03	2.05	1.87	4.95	2.92	1.35
Ho	0.98	1.12	0.25	0.34	0.61	0.38	0.33	0.12	0.79	0.35	0.36	0.30	0.98	0.45	0.23
Er	3.60	4.40	0.85	1.00	2.34	1.27	1.23	0.38	2.95	1.31	1.31	0.91	3.79	1.72	0.72
Tm	0.38	0.41	0.10	0.09	0.29	0.17	0.14	0.04	0.30	0.12	0.32	0.10	0.45	0.19	0.08
Yb	2.68	3.29	0.69	0.89	1.82	1.27	1.15	0.33	2.05	1.01	1.42	1.10	2.89	1.05	0.64
Lu	0.40	0.49	0.10	0.15	0.29	0.24	0.15	0.06	0.34	0.20	0.21	0.09	0.57	0.22	0.11
Hf	6.04	6.84	0.40	0.08	1.02	1.11	0.54	0.29	2.09	0.82	0.76	0.08	2.35	0.85	0.82
Ta	1.43	1.47	0.09	0.10	0.18	0.12	0.09	0.04	0.33	0.07	0.15	0.10	0.23	0.18	0.12
Pb	0.03	0.02	0.63	0.19	0.10	0.06	0.06	0.00	0.28	0.18	0.51	0.12	15.04	0.14	0.10
Th	14.2	17.2	0.81	0.36	0.36	0.23	0.19	0.06	0.94	0.40	1.80	0.38	0.50	0.51	0.60
U	0.34	0.25	0.76	1.20	0.08	0.02	0.14	0.02	1.54	1.34	0.98	0.69	0.15	2.21	1.62
Sc + Y + Zr + Hf (µg/g)	288	336	44.7	55.6	131	113	72.0	24.0	216	127	90.4	64.6	200	130	66.4
$(La/Yb)_N$	9.82	8.82	3.38	2.92	1.09	0.60	0.97	1.24	0.91	2.03	1.35	1.58	1.00	2.09	1.97
$(La/Pr)_N$	1.94	1.85	1.69	0.66	1.13	0.97	0.99	0.99	0.34	0.66	0.48	0.68	1.38	0.43	0.49
Ce*	1.16	1.18	1.25	0.71	0.30	0.31	0.35	0.34	1.32	0.85	3.91	0.78	0.04	2.11	1.25
Eu*	0.69	0.70	0.94	0.74	1.00	0.78	1.03	1.08	0.74	0.70	0.55	0.81	1.19	0.64	0.67
Tm*	0.80	0.70	0.87	0.64	0.91	0.86	0.74	0.71	0.80	0.70	1.51	0.63	0.88	0.90	0.80
Avg. REE_N	48.0	54.1	6.81	10.9	11.5	6.32	6.52	2.30	20.9	10.5	17.0	9.31	17.3	16.7	8.02

Table A.6. Mass fractions of trace elements in 25 'CAT-like' cosmic spherules as determined with LA-ICP-MS (part 2).

	WF18-AD1	WF18-AD2	WF18-AD3	WF18-AD4	WF18-AD5	WF18-AD6	WF18-AD7	WF18-AD8	WF18-AD9	WF18-AD10
Li (µg/g)	<LOD	2.40	2.65	<LOD	<LOD	14.3	<LOD	17.6	<LOD	11.4
Sc	19.9	96.3	35.8	28.1	40.2	38.3	32.6	58.1	23.1	53.2
V	15.3	2.79	1.46	0.31	0.12	0.17	0.94	0.09	0.41	1.48
Cr	6.75	5.43	3.87	<LOD	0.67	<LOD	3.70	<LOD	0.85	2.78
Co	2.02	2.44	<LOD	0.34	<LOD	<LOD	3.31	<LOD	<LOD	1.94
Ni	5.70	14.6	9.47	<LOD	<LOD	<LOD	3.74	<LOD	<LOD	1.83
Zn	12.3	20.9	<LOD	1.60	0.91	1.78	6.94	1.47	1.12	4.19
Rb	0.52	1.69	0.67	<LOD	0.06	0.10	1.13	0.04	<LOD	0.90
Sr	26.5	58.3	19.5	30.0	48.9	34.7	13.2	72.3	21.7	19.5
Y	5.31	13.7	9.62	5.87	7.58	7.21	7.69	8.85	5.18	11.2
Zr	12.2	56.5	23.3	15.4	20.9	25.5	22.2	31.5	15.2	67.8
Nb	1.01	3.77	2.03	0.72	1.62	1.98	1.96	2.90	1.05	4.40
Ba	8.82	17.5	7.89	9.36	11.8	11.0	4.03	27.6	7.97	16.3
La	0.88	5.51	3.03	0.88	1.62	1.00	1.10	1.57	0.86	2.42
Ce	3.47	5.12	2.45	0.95	0.62	0.51	1.86	0.32	0.79	9.52
Pr	0.47	2.26	1.76	0.34	0.53	0.49	0.57	0.28	0.29	1.54
Nd	2.39	10.3	7.88	2.13	2.74	2.16	2.72	1.59	1.56	7.71
Sm	0.95	2.05	1.96	0.46	0.98	0.77	0.86	0.65	0.52	1.84
Eu	0.21	0.77	0.35	0.22	0.32	0.34	0.15	0.47	0.15	0.50
Gd	0.70	1.85	1.83	0.79	1.01	0.98	0.78	0.83	0.78	1.98
Tb	0.12	0.31	0.23	0.14	0.20	0.22	0.14	0.15	0.14	0.31
Dy	0.95	2.00	1.49	0.91	1.31	1.23	1.03	1.40	0.88	1.93
Ho	0.20	0.42	0.39	0.20	0.26	0.25	0.24	0.31	0.19	0.33
Er	0.72	1.05	0.94	0.56	0.74	0.73	0.82	0.92	0.68	1.06
Tm	0.06	0.16	0.12	0.08	0.11	0.05	0.12	0.16	0.07	0.14
Yb	0.64	1.42	1.06	0.68	0.79	1.02	0.65	1.23	0.51	0.99
Lu	0.08	0.18	0.15	0.11	0.12	0.14	0.17	0.11	0.07	0.18
Hf	0.59	2.14	0.62	0.43	0.57	0.73	1.30	1.31	0.43	2.03
Ta	0.06	0.22	0.12	0.06	0.04	0.06	0.08	0.18	0.05	0.24
Pb	0.08	0.11	0.05	0.05	0.10	0.05	0.04	0.05	0.09	0.12
Th	0.20	0.24	0.23	0.10	0.13	0.19	0.20	0.52	0.10	0.56
U	0.09	1.58	0.45	0.02	0.04	0.01	0.33	0.02	0.03	1.47
Sc + Y + Zr + Hf (µg/g)	38.0	169	69.3	49.8	69.3	71.7	63.8	99.8	44.0	134
$(La/Yb)_N$	0.94	2.63	1.95	0.88	1.40	0.67	1.14	0.87	1.14	1.65
$(La/Pr)_N$	0.73	0.95	0.67	1.01	1.19	0.80	0.76	2.17	1.16	0.61
Ce*	1.28	0.36	0.27	0.37	0.16	0.19	0.58	0.11	0.37	1.18
Eu*	0.80	1.20	0.57	1.10	0.99	1.20	0.57	1.93	0.72	0.80
Tm*	0.59	0.88	0.78	0.88	0.94	0.38	1.06	0.97	0.81	0.91
Avg. REE_N	4.17	12.0	8.92	3.66	5.11	4.68	4.66	5.01	3.28	9.92

Table A.7. Oxygen isotope ratio data[3] as determined using SIMS.

Analysis Name	$\delta^{18}O$ (‰)	2SD	$\delta^{17}O$ (‰)	2SD	$\Delta^{17}O$ (‰)	2SD
WF18-0201 @ 1	24.73	0.54	12.74	0.61	-0.12	0.68
WF18-0201 @ 2	25.44	0.42	13.32	0.54	0.09	0.58
WF18-0201 @ 3	26.41	0.39	13.49	0.48	-0.24	0.52
WF18-0201 @ 4	22.12	0.43	11.75	0.63	0.25	0.66
WF18-0201 average	**24.68**		**12.83**		**-0.01**	
WF18-0204 @ 1	39.70	0.39	18.11	0.61	-2.53	0.64
WF18-0204 @ 2	42.12	0.32	20.69	0.56	-1.21	0.58
WF18-0204 @ 3	40.79	0.42	19.48	0.60	-1.73	0.64
WF18-0204 average	**40.87**		**19.43**		**-1.82**	
WF18-0207 @ 1	10.47	0.35	5.25	0.49	-0.19	0.52
WF18-0207 @ 2	9.54	0.30	4.99	0.44	0.02	0.47
WF18-0207 @ 3	4.85	0.37	1.95	0.57	-0.57	0.60
WF18-0207 average	**8.29**		**4.06**		**-0.25**	
WF18-0208 @ 1	46.89	0.40	23.84	0.61	-0.54	0.64
WF18-0208 @ 2	46.46	0.45	23.15	0.57	-1.01	0.62
WF18-0208 @ 3	41.77	0.41	20.78	0.49	-0.94	0.53
WF18-0208 @ 4	46.03	0.36	22.68	0.54	-1.26	0.57
WF18-0208 average	**45.29**		**22.61**		**-0.94**	
WF18-0209 @ 1	38.05	0.43	19.70	0.49	-0.09	0.54
WF18-0209 @ 2	45.84	0.35	23.48	0.63	-0.35	0.66
WF18-0209 @ 3	40.92	0.37	20.08	0.58	-1.20	0.61
WF18-0209 @ 4	34.07	0.70	16.94	0.64	-0.77	0.74
WF18-0209 average	**39.72**		**20.05**		**-0.60**	
WF18-0214 @ 1	-7.01	0.60	-2.22	0.71	1.42	0.78
WF18-0214 average	**-7.01**		**-2.22**		**1.42**	
WF18-0215 @ 1	39.02	0.32	18.61	0.50	-1.68	0.53
WF18-0215 @ 2	38.24	0.35	18.19	0.58	-1.70	0.60
WF18-0215 @ 3	15.05	0.48	8.44	0.68	0.62	0.72
WF18-0215 @ 4	36.99	0.36	17.23	0.56	-2.01	0.59
WF18-0215 @ 5	6.89	0.35	3.59	0.59	0.01	0.62
WF18-0215 average	**27.24**		**13.21**		**-0.95**	
WF18-0221 @ 1	11.09	0.34	5.31	0.59	-0.46	0.61
WF18-0221 @ 2	11.84	0.48	6.15	0.53	0.00	0.59
WF18-0221 @ 3	9.43	0.33	4.80	0.46	-0.11	0.49
WF18-0221 @ 4	10.72	0.37	4.71	0.48	-0.86	0.52
WF18-0221 average	**10.77**		**5.24**		**-0.36**	
WF18-0227 @ 1	57.41	0.39	28.85	0.58	-1.00	0.62
WF18-0227 @ 2	59.70	0.37	29.65	0.57	-1.39	0.61
WF18-0227 @ 3	58.60	0.40	29.44	0.58	-1.03	0.62
WF18-0227 average	**58.57**		**29.31**		**-1.14**	
WF18-0413 @ 1	37.68	0.50	19.96	0.63	0.37	0.68
WF18-0413 @ 2	31.16	0.47	17.08	0.61	0.88	0.65
WF18-0413 @ 3	31.68	0.42	16.36	0.55	-0.11	0.59
WF18-0413 @ 4	32.87	0.70	17.15	0.73	0.06	0.81
WF18-0413 average	**33.35**		**17.64**		**0.30**	

[3] The intermediate precisions of $\delta^{17}O$ and $\delta^{18}O$ are calculated by quadratic propagation of the sample repeatability and reproducibility of the reference material within the analytical session: $2SD = ((2SD_{repeatability})^2 + (2SD_{ref.material}))^{0.5}$. Uncertainties on $\Delta^{17}O$ are calculated as $2SD = ((2SD(\delta^{17}O))^2 + (0.52*2SD(\delta^{18}O))^2)^{0.5}$.

Table A.8. Oxygen isotope data as determined using SIMS (continued).

Analysis Name	$\delta^{18}O$ (‰)	2SD	$\delta^{17}O$ (‰)	2SD	$\Delta^{17}O$ (‰)	2SD
WF18-0403 @ 1	41.92	0.87	23.41	0.67	1.61	0.81
WF18-0403 @ 2	34.86	0.64	19.01	0.55	0.88	0.65
WF18-0403 average	**38.39**		**21.21**		**1.25**	
WF18-0419 @ 1	19.76	0.39	11.32	0.63	1.05	0.66
WF18-0419 @ 2	8.82	0.51	6.42	0.68	1.84	0.73
WF18-0419 @ 3	13.00	0.35	7.03	0.66	0.27	0.69
WF18-0419 average	**13.86**		**8.26**		**1.05**	
WF18-0501 @ 1	13.08	0.32	4.01	0.55	-2.79	0.57
WF18-0501 @ 2	14.32	0.36	4.59	0.61	-2.86	0.64
WF18-0501 @ 3	16.06	0.38	5.33	0.55	-3.02	0.59
WF18-0501 average	**14.49**		**4.64**		**-2.89**	
WF18-0502 @ 1	9.82	0.37	6.04	0.56	0.93	0.59
WF18-0502 @ 2	9.22	0.32	5.75	0.50	0.96	0.53
WF18-0502 average	**9.52**		**5.90**		**0.95**	
WF18-0504 @ 1	7.43	0.35	4.18	0.53	0.32	0.56
WF18-0504 @ 2	9.87	0.31	5.27	0.67	0.14	0.69
WF18-0504 average	**8.65**		**4.73**		**0.23**	
WF18-0505 @ 1	17.92	0.34	5.93	0.59	-3.39	0.61
WF18-0505 @ 2	17.37	0.30	6.43	0.61	-2.60	0.63
WF18-0505 average	**17.65**		**6.18**		**-3.00**	
WF18-0506 @ 1	13.52	0.38	5.58	0.62	-1.45	0.65
WF18-0506 @ 2	15.50	0.35	5.58	0.58	-2.48	0.61
WF18-0506 @ 3	12.85	0.36	5.24	0.67	-1.45	0.70
WF18-0506 @ 4	15.96	0.28	5.77	0.49	-2.52	0.52
WF18-0506 average	**14.46**		**5.54**		**-1.98**	
WF18-0507 @ 1	50.64	0.33	28.69	0.54	2.35	0.57
WF18-0507 @ 2	51.42	0.40	29.82	0.55	3.08	0.59
WF18-0507 @ 3	51.23	0.30	28.07	0.62	1.43	0.64
WF18-0507 average	**51.10**		**28.86**		**2.29**	
WF18-0508 @ 1	26.62	0.35	15.25	0.51	1.41	0.54
WF18-0508 @ 2	26.38	0.36	15.60	0.62	1.89	0.64
WF18-0508 @ 3	29.08	0.37	16.40	0.60	1.27	0.63
WF18-0508 average	**27.36**		**15.75**		**1.52**	
WF18-0509 @ 1	12.41	0.33	7.35	0.53	0.90	0.55
WF18-0509 average	**12.41**		**7.35**		**0.90**	
WF18-0512 @ 1	35.93	0.34	16.88	0.54	-1.81	0.57
WF18-0512 @ 2	39.43	0.36	18.42	0.58	-2.09	0.61
WF18-0512 @ 3	39.77	0.33	18.55	0.55	-2.13	0.57
WF18-0512 average	**38.38**		**17.95**		**-2.01**	
WF18-0513 @ 1	23.17	0.33	10.35	0.56	-1.70	0.59
WF18-0513 @ 2	21.88	0.44	9.98	0.47	-1.40	0.53
WF18-0513 average	**22.53**		**10.17**		**-1.55**	
WF18-0514 @ 1	17.27	0.37	4.92	0.59	-4.06	0.62
WF18-0514 @ 2	18.57	0.36	6.75	0.61	-2.91	0.64
WF18-0514 average	**17.92**		**5.84**		**-3.49**	

Conflict of interest statement

We, the authors, hereby declare that there are no conflicts of interest to declare. There is no financial interest to report. We certify that the submission is original work and is not under review at any other publication.